

Article

YS3AM: Adaptive 3D Reconstruction and Harvesting Target Detection for Clustered Green Asparagus

Si Mu ^{1,2}, Jian Liu ¹, Ping Zhang ³, Jin Yuan ^{1,*}  and Xuemei Liu ¹ 

¹ College of Mechanical & Electronic Engineering, Shandong Agricultural University, Tai'an 271018, China; lxmywj@126.com (X.L.)

² Dezhou Vocational and Technical College, Dezhou 253000, China

³ College of Information Science and Engineering, Shandong Agricultural University, Tai'an 271018, China

* Correspondence: jyuan@sda.edu.cn

Abstract: Green asparagus grows in clusters, which can cause overlaps with weeds and immature stems, making it difficult to identify suitable harvest targets and cutting points. Extracting precise stem details in complex spatial arrangements is a challenge. This paper explored the YS3AM (Yolo-SAM-3D-Adaptive-Modeling) method for detecting green asparagus and performing 3D adaptive-section modeling using a depth camera, which could benefit harvesting path planning for selective harvesting robots. Firstly, the model was developed and deployed to extract bounding boxes for individual asparagus stems within clusters. Secondly, the stems inside these bounding boxes were segmented, and binary masks were generated. Thirdly, high-quality depth images were obtained through pixel block completion. Finally, a novel 3D reconstruction method, based on adaptive section modeling and combining the mask and depth data, is proposed. And an evaluation method is introduced to assess modeling accuracy. Experimental validation showed high-performance detection (1095 field images demonstrated, Precision: 98.75%, Recall: 95.46%, F1: 0.97) and robust 3D modeling (103 asparagus stems, average RMSE: length 0.74, depth: 1.105) under varying illumination conditions. The system achieved 22 ms per stem processing speed, enabling real-time operation. The results demonstrated that the 3D model accurately represents the spatial distribution of clustered green asparagus, enabling precise identification of harvest targets and cutting points. This model provided essential spatial pathways for end-effector path planning, thereby fulfilling the operational requirements for efficient green asparagus harvesting robots.



Academic Editor: Valentin Vlăduț

Received: 2 January 2025

Revised: 3 February 2025

Accepted: 10 February 2025

Published: 14 February 2025

Citation: Mu, S.; Liu, J.; Zhang, P.; Yuan, J.; Liu, X. YS3AM: Adaptive 3D Reconstruction and Harvesting Target Detection for Clustered Green Asparagus. *Agriculture* **2025**, *15*, 407. <https://doi.org/10.3390/agriculture15040407>

Copyright: © 2025 by the authors. Licensee MDPI, Basel, Switzerland. This article is an open access article distributed under the terms and conditions of the Creative Commons Attribution (CC BY) license (<https://creativecommons.org/licenses/by/4.0/>).

1. Introduction

Harvesting green asparagus is the most labor-intensive part of its production cycle [1], primarily relying on manual labor in China, which accounts for about 50% of production costs. Therefore, a harvesting robot capable of automatically harvesting green asparagus would significantly enhance productivity [2]. However, accurate identification and segmentation and efficient harvesting of green asparagus struggle meet the demands of operating equipment due to factors such as light fluctuations, plant overlap, camera angle, and distance, all which impact target detection in outdoor-grown green asparagus [3]. Estimating spatial positions and key-points of harvesting objects is also a crucial technical challenge in computer vision and provides important information for robotic harvesting. Thus, the

accurate identification of asparagus clusters and the construction of 3D growth models in unstructured environments are vital for non-destructive green asparagus harvesting.

Various imaging systems and AI-based image processing techniques offer a potential solution for accurately and reliably monitoring green asparagus growth and automated asparagus harvesting [4–7]. Irie et al. [8] proposed a harvesting robot that measured green asparagus cross-section using a 3D vision sensor. Outdoor fruit and vegetable image recognition and localization are greatly affected by sunlight intensity and color temperature. For instance, one Japanese study [9] employed dual laser sensors to avoid light interference while detecting and positioning asparagus stems, ensuring reliable performance in varying light conditions.

With the development of Convolutional Neural Networks (CNNs), deep learning technology has shown great potential for detecting clustered green asparagus outdoors [10]. M. Peebles et al. [11] utilized Faster R-CNN (F-RCNN) [12] to detect green asparagus features in outdoor RGB images, researching the optimal network architecture for asparagus detection. Li et al. [13] proposed a recognition method that combined image preprocessing with the LeNet [14] network for autonomous harvesting of green asparagus under natural outdoor lighting conditions. Hong et al. [15,16] improved the YOLOv5 algorithm to enhance feature propagation and reusability, focusing on asparagus growth characteristics.

The target detection algorithms mentioned performed well in simple backgrounds. However, outdoor green asparagus typically grows in irregular clusters of 3–6 stems, often overlapping with obstacles like steel rods, mother asparagus and immature asparagus, which complicates detection and reduces harvesting efficiency [17]. Recent advancements in depth image-based recognition have shown promise for improving the detection of clustered fruits and vegetables in complex environments [18]. This technique utilized depth information based on the 2D shape of the cluster region to achieve recognition of each fruit and vegetable object in the cluster region. The method could have good recognition performance in the presence of mild occlusion of fruits and vegetables, but there have been fewer studies related to green asparagus in clusters. Leu et al. [19] developed a harvesting robot using an RGB-D vision sensor to capture the 3D positions of green asparagus, effectively utilizing depth data. Kennedy et al. [20] introduced a ground-plane projection method combining multiple monocular cameras for better performance in green asparagus harvesting. Wang et al. [16] further refined the YOLACT++ algorithm for determining cutting points at the base of mature asparagus. Mu et al. [21] proposed the S2CPL model, which uses RGB-D sensors to evaluate selective harvesting suitability and accurately locate subsoil cutting points. Despite these advancements, the precision of point localization remains a challenge, especially when compared to models that incorporate the entire asparagus stem structure. This limitation could negatively affect the integrity of harvesting path planning, particularly in densely clustered asparagus patches.

The development of 3D models holds significant potential for improving the planning of harvesting paths and aiding the construction of stable, autonomous fruit-picking robots [2,22]. Yoshida et al. [23] proposed a recognition method that utilizes RGB-D cameras to capture 3D information of pears and apples grown on joint V-shaped trellises. This method simulates the fruits into spheres in 3D space using circular fitting. Ma et al. [24] focused on the reconstruction of 3D crop models using RGB-D binocular vision, employing a triangulation algorithm based on the greedy projection method for model generation. Magistri et al. [25] proposed a pipeline that leverages high-resolution 3D data during the learning phase, enabling contrastive 3D shape completion and reconstruction for agricultural robots using RGB-D frames. In agricultural activities, LiDAR (Light Detection and Ranging) has also been used to create accurate and quantifiable models of plant structures. For example, Omasa et al. [26] employed LiDAR with a pulse density of ~30 pulses m⁻²

to estimate tree height in Japanese coniferous and broadleaved forests. Herrero-Huerta et al. [27] monitored leaf movement in indoor plants using terrestrial LiDAR. Although these studies highlight significant advancements in RGB-D and LiDAR-based 3D modeling for various crops, to the best of our knowledge, there is currently no dedicated research on the 3D modeling of green asparagus.

Extracting complex spatial position information of clustered green asparagus stems presents a significant challenge in identifying suitable harvest targets and high-precision cutting points. A novel combined detection network and 3D reconstruction model named YS3AM (Yolo-SAM-3D-Adaptive-Modeling) is proposed to address these challenges by detecting clustered green asparagus and constructing detailed 3D visual models in unstructured environments. The main contributions of this paper are as follows:

- (1) The YS3AM model combines enhanced YOLOv7 and SAM algorithms to more accurately segment asparagus stems in clusters, improving detection performance in complex environments.
- (2) By using an improved pixel dilation algorithm, YS3AM models can process incomplete depth data from RGB-D sensors, ensuring a more robust and accurate 3D model reconstruction.
- (3) YS3AM integrates stem masks with depth images to create adaptive-section 3D models that enable efficient path planning for harvesting in unstructured environments.

2. Materials and Methods

2.1. Overview

The YS3AM model was composed of five principal components, as shown in Figure 1.

- (1) Through field investigations, the growth patterns and structural characteristics of green asparagus were carefully studied. RGB-D images of clustered green asparagus were captured using an RGB-D sensor (Figure 1a).
- (2) Using a deep detection model, each green asparagus stem in the augmented images was identified as a separate object. Semantic segmentation was then applied to generate precise masks for each asparagus stem (Figure 1b).
- (3) Missing depth pixels were filled by combining the semantic masks with the depth images captured by the camera, resulting in a complete depth map. The contours of the asparagus stems were then extracted, and the 3D coordinates of some key points along the stems were calculated through coordinate transformation from the pixel coordinate system to the camera coordinate system (Figure 1c).
- (4) Fitting the stalk curves based on the concept of equal segmentation, each stalk segment was considered as a cylinder. The length, center, and radius of each section were calculated, and by combining the approximate cylinders of each asparagus section, a complete 3D model of each asparagus stalk was constructed (Figure 1d).
- (5) An adaptive-section modeling method was proposed to dynamically adjust segmentation based on the length of the asparagus stems. To evaluate the model's precision, the Root Mean Square Error (RMSE) index was introduced, measuring the offsets of selected key points and providing a reliable assessment of the 3D spatial model's accuracy (Figure 1e).

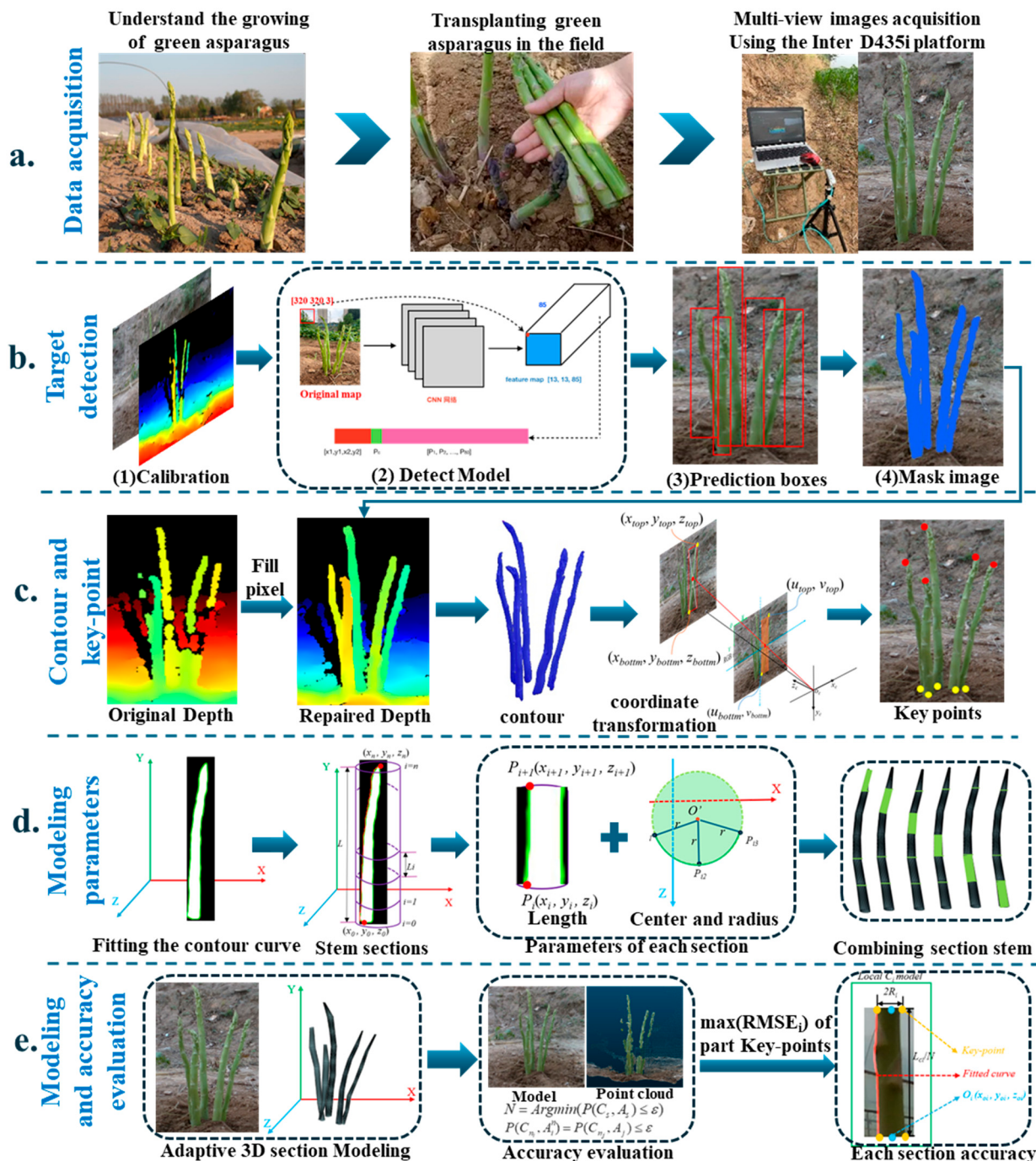


Figure 1. Methodology flow chart.

2.2. Experimental Data

At present, there are many large-scale asparagus plantations throughout the country. After conducting field surveys, we found that green asparagus was planted in the soil ridge with a height of 15–20 cm, planting row spacing of 1.2–1.8 m, plant spacing of 20–25 cm, and the diameter of each stem was 1.5–2 cm. The growth rate during the peak growth period is about 20 cm/d and the growth is relatively dense. This high density of stem conditions presents additional challenges for the machine vision systems, as harvesting targets are heavily obscured by weeds or immature asparagus.

2.2.1. Data Acquisition

The data of green asparagus in this paper were acquired in July 2024, which was not the harvest period of green asparagus. Therefore, green asparagus grown outdoors was transplanted to two experimental farms at Panhe Campus of Shandong Agricultural University for outdoor simulation experiments. The image data used in this paper were acquired using an RGB-D sensor, RealSense D435i (Intel, Santa Clara, CA, USA), under both cloudy and sunny weather conditions. The collection periods included 7 a.m. to acquire green asparagus images in a low-light environment, and 5:30 p.m. to the sundown. During these two periods, the camera collected a total of 730 original data, including 3182 green asparagus plants. To better simulate the visual system during the picking robot operation, we collected the images from multiple directions, and there were many large-area occlusion and coincidence phenomena in the image, including the fact that the head, middle, and bottom were occluded. The specific images are shown in Figure 2.



Figure 2. Green asparagus images collected in different light conditions and at different angles.

2.2.2. Dataset Preparation

YS3AM was a multi-task network; it was required to detect the green asparagus prediction box, key points, and their 3D positions. There were two types of data or dataset, namely RGB-D data and point cloud data. The RGB-D data were obtained by camera directly. The RGB-D data consisted of four channels, the R, G, B channel for green asparagus segmentation and KeyPoints detection, and the key points on the RGB image as an index in the depth image to read the depth value. This point cloud data was used to evaluate the model performance of 3D reconstruction.

(1) Labelling bounding boxes and Data augmentation

During the dataset creation phase, all target green asparagus in RGB images form RGB-D data were labeled using LabelImg v1.8.1 (<https://github.com/tzutalin/labelImg> (accessed on 1 July 2024)), excluding those with occlusions exceeding two-thirds. To enhance the persuasiveness of the experimental results, this paper employed Augmentor

(0.6.6) and Imgaug (0.4.0) [28] to expand the dataset. Given the uneven outdoor terrain and the potential for blurring due to equipment movement, techniques like chamfer, gamma transformation, dilation, and Gaussian noise were used to realistically simulate the growth environment. The datasets were collected in sunny and cloudy conditions, and effects like rain, snow, fog, and clouds were added to simulate various weather scenarios, increasing dataset diversity. Six augmentation methods were randomly applied to single images (Figure 3), resulting in the Sunny dataset expanding from 388 to 2328 images, totaling 10,488 green asparagus, while the Cloudy dataset grew from 342 to 2052 images, containing 8604 green asparagus. Both datasets were randomly divided into training and testing sets in a 3:1 ratio, with the details shown in Table 1. In the first row of the table, “Images” refers to the total number of images collected under sunny and cloudy conditions, and “Instances” indicates the total number of labeled asparagus stems within the respective images. To reduce training complexity, the resolution of training images was adjusted to 640×640 .

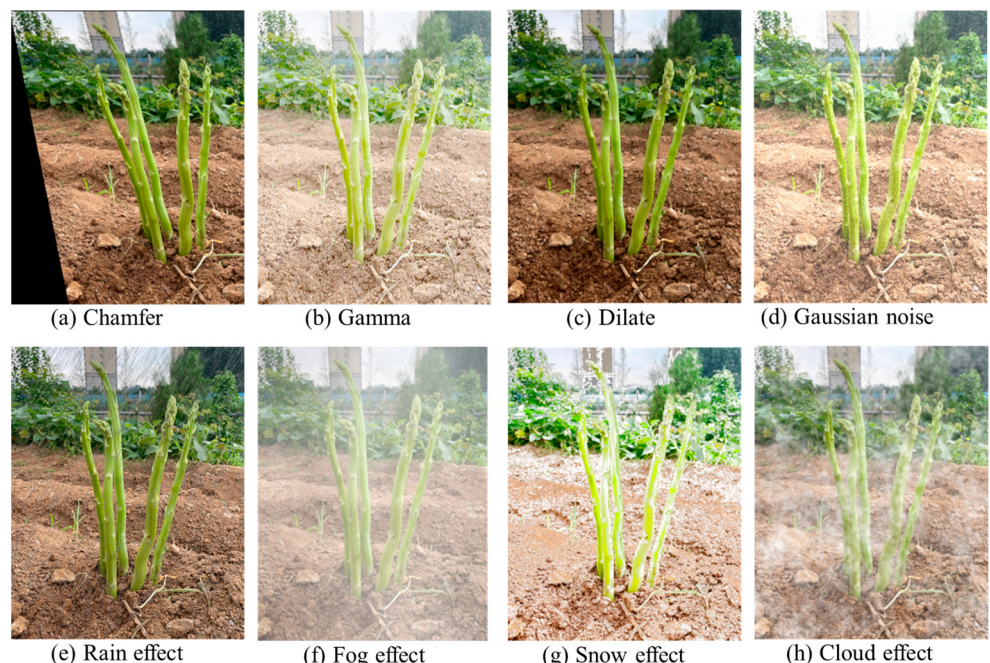


Figure 3. Some augmentation effects of green asparagus.

Table 1. Dataset division.

Data Set	Training Images/Instances	Testing Images/Instances	Total Images/Instances
Sunny	1746/7888	582/2600	2328/10,488
Cloudy	1539/6353	513/2251	2052/8604
Total	3285/14,241	1095/4851	4380/19,092

(2) Generating color point cloud

The point cloud data were generated by RGB image, internal parameters of the camera, and a depth image. The coordinate value (u, v) in the pixel coordinate system were used to find the depth value z on the depth image, and Equation (1) was used for deprojecting and calculating the coordinate value (x, y, z) in the camera coordinate system. And K is a 3×3 matrix containing the internal parameters of the camera.

$$\begin{bmatrix} x \\ y \\ z \end{bmatrix} = zK \begin{bmatrix} u \\ v \\ 1 \end{bmatrix} \quad (1)$$

When all pixels were processed as above, a point cloud was generated. This full point cloud is just used to evaluate the results of 3D model detection. For effective consideration, during detection, only the (x, y, z) coordinates of some key-points in green asparagus were calculated. The subsequent 3D model results are described in the following chapters.

2.3. The Prediction Box Detection of Green Asparagus Stem

In the top-down detection mode, the small image containing a whole asparagus stem must be acquired. And the segmentation results of the stem are highly dependent on the prediction box detection results. In the natural environment, the background interference is very strong. Therefore, the prediction box detection network must have a strong background exclusion ability.

Based on the application of the target detection algorithm mentioned in Section 1 in agriculture, the YOLO series network has a strong real-time detection speed. YOLOv7 [29] is one of the most advanced single-stage target detection algorithms, which balances the conflict between the number of parameters, computational consumption, and performance, and achieves satisfactory results in terms of both speed and accuracy. In this paper, YOLOv7 served as the primary benchmark architecture, and a new design idea was proposed to solve problems such as the large number of targets under observation, the different shapes and sizes of the stem at each growth stage, and many large-area occlusion and coincidence phenomena in the actual detection application. Specific improvements were made in the following four aspects:

(1) The lightweight CBH-S module

The SiLu function of the CBS convolution block in the original model, also known as the Swish activation function, is an adaptive activation function. The Swish activation function has the characteristics of no upper bound and lower bound, smoothness and non-monotonicity, which improves the accuracy of the original model to a certain extent and alleviates the problem of gradient disappearance. However, it is computationally expensive, with complex derivations and slow quantization. To address this, the CBH-S module was introduced to reduce the computational cost while maintaining accuracy. The Swish activation function was replaced with the more efficient HardSwish function, reducing computation by using a segmented linear function instead of the exponential Sigmoid function, as shown in Equation (2).

$$HardSwish(x) = \begin{cases} 0 & x \leq -3 \\ x & x \geq 3 \\ x \frac{ReLU6(x+3)}{6} & otherwise \end{cases} \quad (2)$$

(2) Heavily parameterized ultra-lightweight feature extraction module

Feature reuse is a key technique in lightweight convolutional neural network design. The MobileOne ultra-lightweight network module [30] replaced the ELAN module of the YOLOv7 backbone to achieve heavy parameterization and ultra-lightweight network architecture. MobileOne (Figure 4) enabled the extraction of rich feature information from green asparagus, including cases of occlusion by roots or other asparagus stems. During the network training, the deep convolution of MobileOne made it possible to obtain a larger sensory field at different scales by 3×3 convolution kernel. By constructing multiple paths on different levels, each channel of the detected green asparagus feature map had certain

information exchange, and the feature information of the lower layer is complemented with the richer feature information of the previous layers.

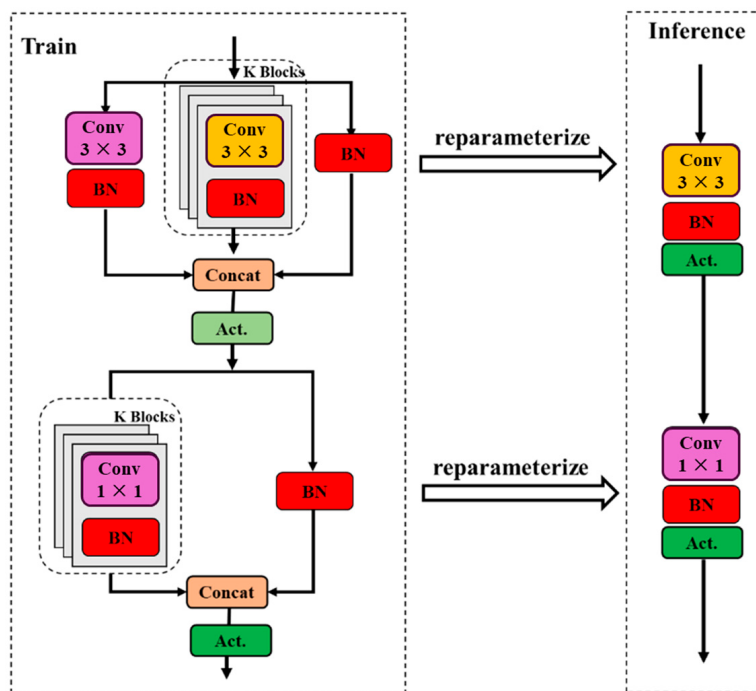


Figure 4. The building block of MobileOne.

(3) Lightweight Multi-path Convolution

Previous attention mechanisms primarily focused on encoding inter-channel information, often neglecting the importance of location information. Hou et al. [31] proposed a novel mobile network attention mechanism for lightweight networks, which embedded location information into channel attention, called CoordAttention (CA).

In the feature fusion stage, two transition modules, MPConv, were improved. The improved MPConv structure is shown in Figure 5b. The CA attention mechanism replaced the 1×1 convolution in the second branch of the MPConv module, which could reduce both the feature loss caused by the network feature processing and the computational overhead of the mobile device by accurately locating and identifying the target area. Additionally, a CBH-S convolutional module with step size of $2, 3 \times 3$ and a CBH-S convolutional module with step size of $1, 1 \times 1$ was used to replace the Conv module, which was able to reduce the calculation amount and ensure the model had a better performance.

(4) Cross-Scale Integration Strategy

Multi-scale fusion allows the network to capture object details and features at various scales, improving target detection and recognition. To enhance the network's ability to extract features from green asparagus and adapt to lighting and scale changes, a cross-scale fusion strategy was proposed in this paper, as shown by the red dashed arrows in Figure 6. This strategy integrates shallow feature extraction with deep network semantic information, improving the model's feature extraction capability. This strategy integrates shallow feature extraction with deep network semantic information, improving the model's feature extraction capability.

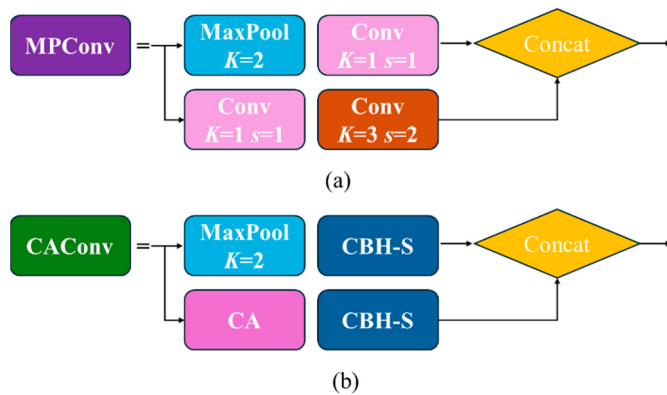


Figure 5. CAConv. (a) MPConv. (b) Improved CAConv.

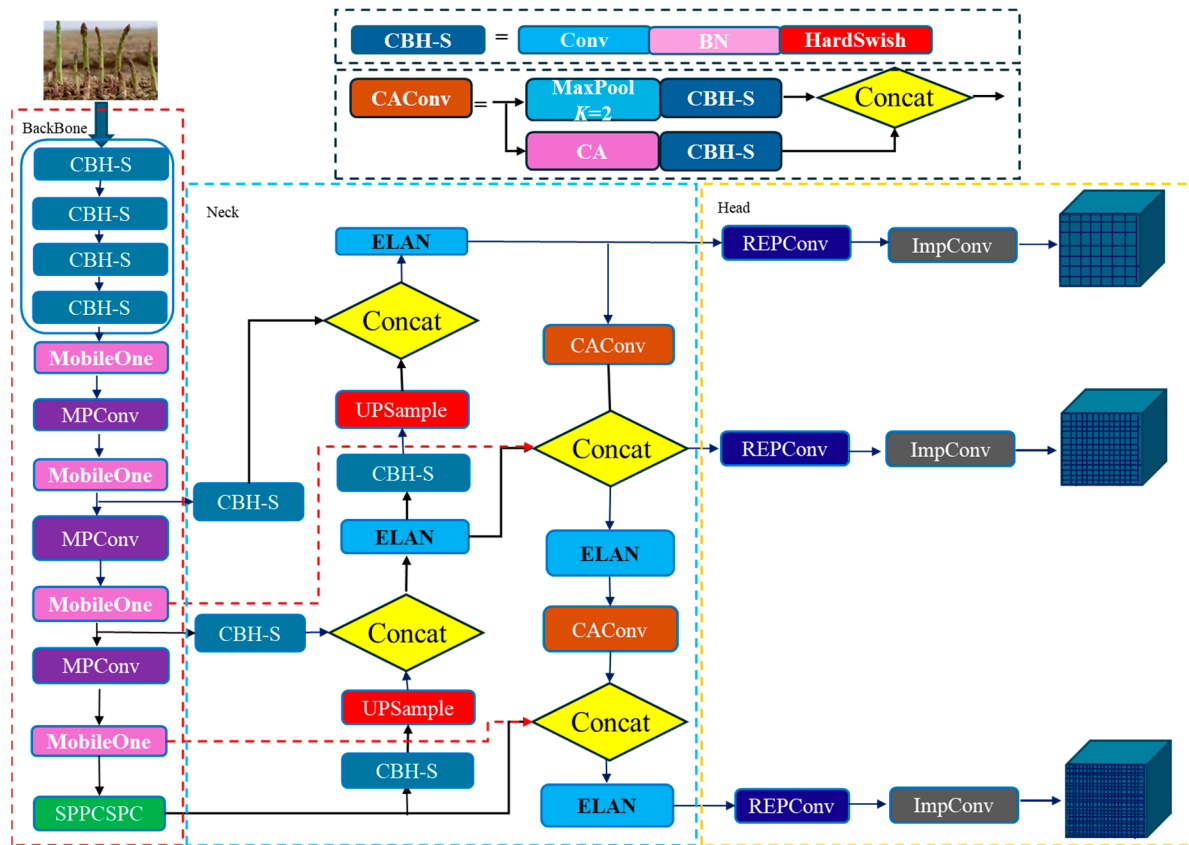


Figure 6. The improved YOLOv7.

The overall improved YOLOv7 model is shown in Figure 6.

2.4. Image Segmentation Network Architectures for Green Asparagus

After the improved YOLOv7 detected the RGB images captured by the depth camera, prediction boxes for each asparagus stem were obtained. Subsequently, the Segment Anything Model (SAM) was employed to detect and segment the green asparagus stem clusters.

SAM [32,33] is a large-scale innovative model developed by Facebook Research in 2023 for general segmentation tasks in computer vision. Trained on a large dataset, SAM can segment (cut out) any morphological feature in any given image, identifying which pixels belong to an object. SAM comprises a vision transformer-based image encoder, a prompt encoder, and a lightweight mask decoder. The image encoder consists of a mask-based autoencoder [34] and a pre-trained vision transformer model [32]. Prompt Encoder (Prompt Encoder) has two categories: sparse (points, boxes, text) and dense (mask). Points and

boxes can be represented by location coding, which combines learning embeddings from each prompt and arbitrary forms of text (processed using a multimodal pre-trained neural network CLIP). The mask is then combined with the image elements after being embedded by convolution. The lightweight mask decoder can effectively map image encoding, prompt encoding, and output tokens to the mask. The decoder of the SAM model is based on the decoder block of Transformer, and the dynamic mask prediction head is added after the decoder. The modified decoder block uses prompt self-attention and cross-attention in both the prompt-to-image embedding direction and vice versa. After running both blocks, the image coding is up-sampled and then the output labeled tokens are mapped to the dynamic linear classifier using MLP. And finally, the dynamic linear classifier calculates the mask prospect probability for each image location.

To handle potential segmentation errors (false positives and false negatives), we implemented several post-processing techniques. First, morphological operations such as opening and closing were applied to remove small noise regions and fill holes in the segmentation masks. Second, the confidence threshold of the segmentation model was adjusted to balance false positives and false negatives. Third, manual verification was introduced for critical frames or regions to ensure the accuracy of the segmentation results, especially at the edges of the asparagus stems.

The transfer learning was utilized to test the detection boxes obtained by the improved YOLOv7 with the weights generated by the base segmentation model SAM on the SA-1B dataset without additional training. The chosen task was semantic segmentation, i.e., dividing the pixels of each image into two different semantic categories: green asparagus (foreground) and background. The process of recognition and semantic segmentation for a natural color image of outdoor green asparagus captured by depth camera (Intel RealSense D435i) is shown in Figure 7. While SAM was not specifically trained for green asparagus images, it successfully captured all major features in the image, demonstrating its effectiveness. Furthermore, accessing the geometric features of the mask allowed for additional feature extraction of green asparagus.

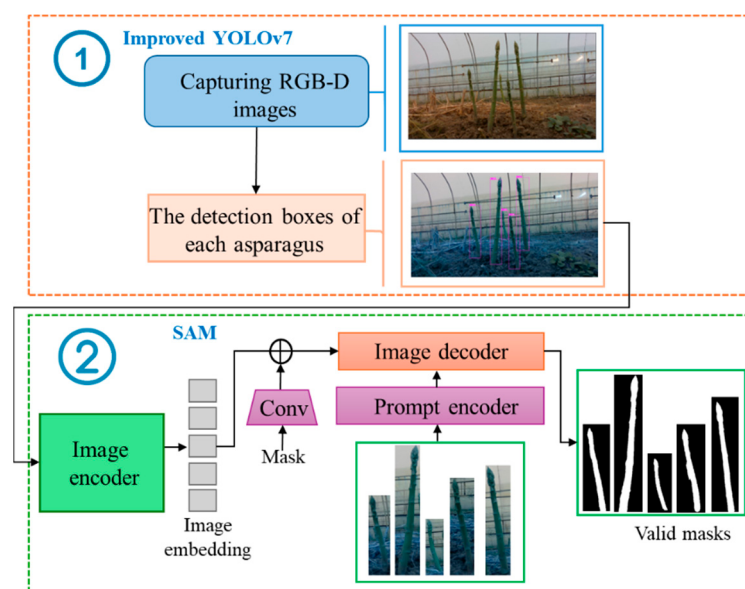


Figure 7. Recognition and semantic segmentation of green asparagus.

2.5. Extracting Space Coordinates for Green Asparagus Stem Using Pixel Mapping

After segmenting green asparagus in the images, the SAM model output their binary mask and mapped it to the corresponding depth image to determine the area where the target was located. However, the initial depth data obtained in the unstructured environment was often mixed with noise and pixel information loss. The dense and noisy initial depth image must pass through a series of preprocessing steps before being used for subsequent analysis and calculations.

2.5.1. Mask-Based Deep Pixel Block Completion

To address the limitations of the RealSense D435i, which include missing depth pixels and noise caused by reflections, semi-transparent or dark objects, and out-of-range measurements, we implemented an improved pixel dilation method based on the IP_BASIC algorithm [35]. This process fills missing pixel blocks in depth data, reducing noise and improving the accuracy of subsequent computations. The specific process is as follows:

(1) Capturing and Aligning Depth Images

The depth camera was positioned forward to capture outdoor images of green asparagus. A distance threshold of 2 m was set to filter out distant background, and the depth images were aligned with the RGB images (Figure 8a). After capturing and aligning the images, the RGB images undergo segmentation to identify individual green asparagus stems (Figure 8b).

(2) Segmentation and Color Space Conversion

The captured RGB images were automatically segmented to create masks for each green asparagus. A pseudo-color was added to the depth map, which was then converted from RGB to HSV color space, separating the H, S, and V components into three independent grayscale images (Figure 8c). Due to light interference, particularly reflections and shadows when capturing green asparagus, the V component was chosen to eliminate darker and oversaturated pixels.

With the masks for each asparagus stem prepared, noise and fine details along the edges were reduced to facilitate pixel expansion in subsequent steps.

(3) Noise Reduction through Mask Erosion

The mask images for each green asparagus underwent erosion with a 3×3 elliptical kernel to reduce fine noise and details at the edges (Figure 8d). After noise reduction, the focus shifted to filling in missing pixels in the depth map.

(4) Pixel Expansion to Fill Missing Depth Data

Effective pixels in the depth map were expanded to fill in missing pixels using a 9×9 elliptical kernels. This step closed black holes along the edges of the masks (Figure 8d). After erosion and expansion, a dense depth map was obtained for subsequent processing (Figure 8e).

The pseudocode for pixel block completion is presented in Algorithm 1. The RGB image (*RGBImg*), depth image (*DepthImg*), and mask image (*MaskImg*) were obtained from the RGB-D sensor. The YS3AM algorithm processes *RGBImg* to generate *MaskImg*. The *DepthImg* was converted to HSV space (*Depth_hsv_img*), and the V channel was selected to create the processed depth image (*Processed_DepthImg*). Next, the maximum iteration count (Max_Iterations) and threshold (Threshold) are defined, and *Processed_DepthImg* was assigned to a temporary depth map (*tempDepthMap*). For each pixel (i, j) in *DepthImg* that was null, it checked whether *MaskImg*[i][j] was marked as an object (OBJECT). If it was, the neighboring pixel values (neighbors) were retrieved, and valid depth values (validDepths) were filtered out. A function named *reduce_noise* was created to apply erosion to the mask

image. Another function named `fill_missing_pixels` was created to fill in the missing pixels in the depth image using dilation. If the maximum difference between `tempDepthMap` and `DepthImg` was less than Threshold, the loop ended. Finally, the processed depth map (`completedDepthMap`) was returned.

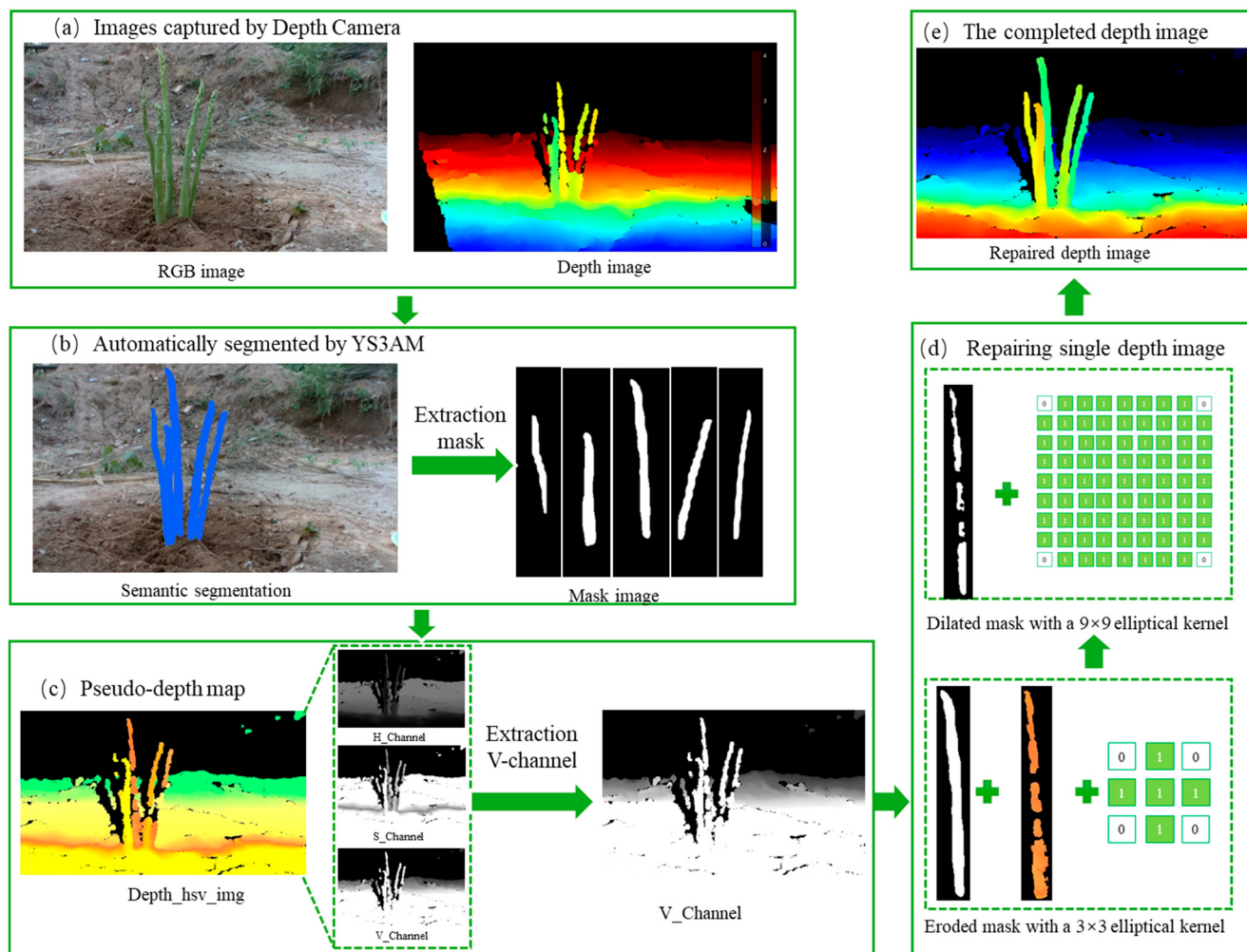


Figure 8. Pixel block completion for depth image.

2.5.2. The Positional Transformation Relationship of Spatial Points of Clustered Green Asparagus

Before establishing the mapping relationship between the 2D images and the depth image, the camera was calibrated to obtain its internal and external parameters, such as the focal length, translation vector, and rotation matrix.

First, an RGB-D image was split into an RGB image and a depth image. As shown in Figure 1, the RGB image (Figure 1a) was fed to the detect network (Figure 1b), and the prediction boxes of the stem were generated. The evaluation metrics and results of prediction box detection are shown in Section 3.1. Then, according to these predicted prediction boxes, each small image containing one asparagus stem was fed into SAM to segment the green asparagus stem from the background. Finally, the contour of green asparagus in pixel coordinates could be obtained through OpenCV. Because the depth image was aligned to the RGB image, the pixel coordinates (U, V) of the contour on the image could be used as the index to find the corresponding depth value.

The mapping relationship between the 2D image and depth image can establish the spatial mapping relationship between the pixel and camera coordinate systems. Based on the principle of binocular visual localization, we used the depth camera intrinsic parameters to convert the contour area detected by the model to space coordinates. The mapping relationship is expressed as follows:

$$\begin{cases} x_i = z_i \frac{u_i - U_x}{f_x} \\ y_i = z_i \frac{v_i - U_y}{f_y} \\ z_i = \frac{D(u_i, v_i)}{c_f} \end{cases} \quad (3)$$

where (x_i, y_i, z_i) are the 3D coordinates of pixel i in camera coordinates; (u_i, v_i) are the pixel coordinates of pixel i ; D is the depth image; c_f is the depth scale factor of the camera; (U_x, U_y) are the pixel coordinates of the IR camera principal point; and (f_x, f_y) are the focal lengths of the IR camera. The positional relationship of spatial points in the camera coordinate system is shown in Figure 9.

Algorithm 1: Pixel block completion

1. $MaskImg \leftarrow YS3AM(RGBImg);$
2. $Depth_hsv_img \leftarrow \text{convert_to_hsv}(DepthImg);$
3. $H_channel, S_channel, V_channel \leftarrow \text{split_hsv_channels}(Depth_hsv_img);$
4. $Processed_DepthImg \leftarrow \text{filter_depth_image}(V_channel, DepthImg);$
5. $\text{tempDepthMap} \leftarrow Processed_DepthImg;$
6. **for** iteration $\leftarrow 1$ to Max_Iterations **do**
7. **for** each pixel (i, j) in $DepthImg$ **do**
8. **if** $MaskImg[i][j] == \text{OBJECT}$ **then**
9. $\text{neighbors} \leftarrow \text{getNeighbors}(\text{tempDepthMap}, i, j);$
10. $\text{validDepths} \leftarrow \text{filterValidDepths}(\text{neighbors});$
11. **if** validDepths is not empty **then**
12. $\text{eroded_MaskImg}[i][j] \leftarrow \text{reduce_noise}(MaskImg, \text{tempDepthMap}[i][j],$
EROSION_KERNEL_SIZE);
13. $\text{dilated_depth_image} \leftarrow \text{fill_missing_pixels}(\text{tempDepthMap}[i][j],$
DILATION_KERNEL_SIZE, $\text{eroded_MaskImg}[i][j]);$
14. $\text{tempDepthMap}[i][j] \leftarrow \text{average}(\text{dilated_depth_image}[i][j]);$
15. **end if**
16. **end if**
17. **end for**
18. **if** $\text{maxDifference}(\text{tempDepthMap}, DepthImg) < \text{Threshold}$ **then**
19. break;
20. **end if**
21. **end for**
22. **return** tempDepthMap **as** completedDepthMap;

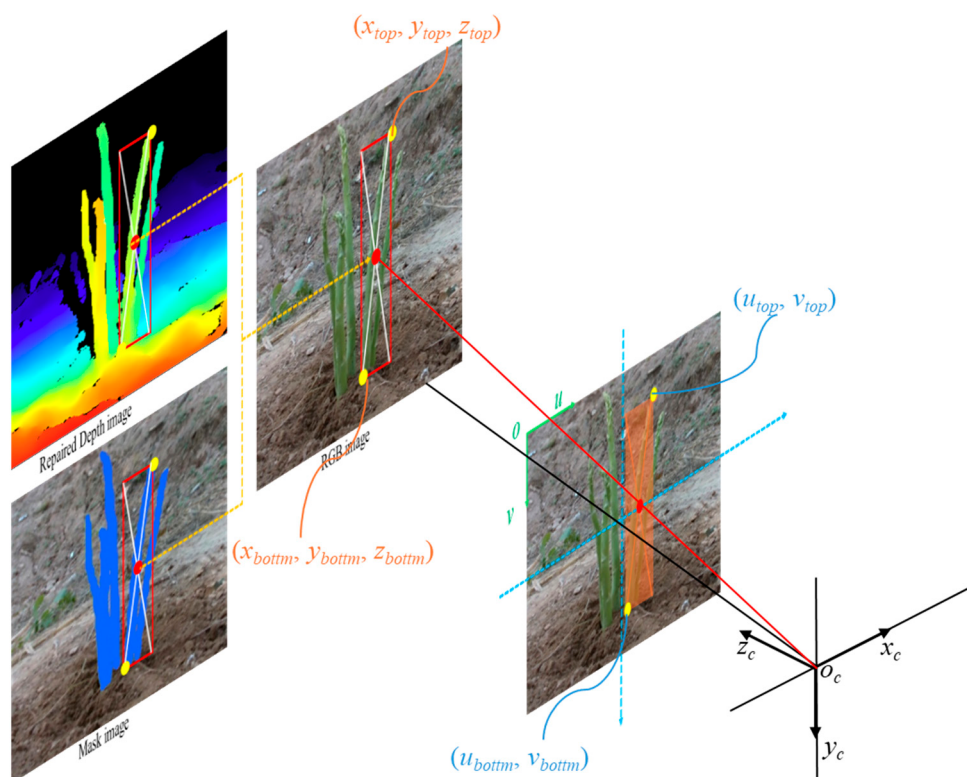


Figure 9. Coordinate transformation of pixel points of green asparagus stems.

2.6. Adaptive-Section Modeling of Clustered Green Asparagus Stems

2.6.1. Visual 3D Section Modeling Approach

Rapid 3D modeling of green asparagus is crucial for efficient harvesting path planning. However, the varying thicknesses, tilting postures, and bending directions of the stems can lead to excessive computational demands if modeled too precisely, impacting efficiency and speed. Voxel modeling offers a more efficient solution by using fixed-length cubes to represent spatial point clouds. Given the upward growth and simple structure of green asparagus, voxel-like geometric modeling is ideal for balancing efficiency and accuracy. We used a cylindrical structure as the basic element, dividing each asparagus into N sections and combining these cylinders to create a precise 3D model of clustered asparagus.

This approach lays the groundwork for effective harvesting planning, and effectively captures the key geometric features of asparagus stems, providing an efficient way to represent their structure. In practical applications, particularly for robotic harvesting, high computational efficiency is crucial. While more detailed models, such as free-form meshes or polyhedra, could offer greater accuracy, these models would introduce significant computational overheads. Given the relatively simple geometric characteristics of green asparagus, cylindrical modeling offers a practical compromise between computational efficiency and the accuracy required for path planning.

As shown in Figure 10, through the network structure mentioned earlier, clusters of green asparagus could be identified and localized and undergo semantic segmentation, and the mask of each green asparagus could be detected by prediction boxes. The binary mask images were instrumental in extracting stem parameters, including the 2D coordinates of the bottom, the tip and the key point of the asparagus stem. These coordinates served as the projection of the three-dimensional object on the camera plane. Utilizing the alignment capabilities of an RGB-D sensor, these 2D coordinates were fused with depth information to determine the depth $D_{u,v}$ of the point $P_{u,v}$ in the camera space. $D_{u,v}$ was then converted to

obtain the Z-axis coordinates in the camera coordinate system, yielding the spatial position information $P(x, y, z)$ of point P .

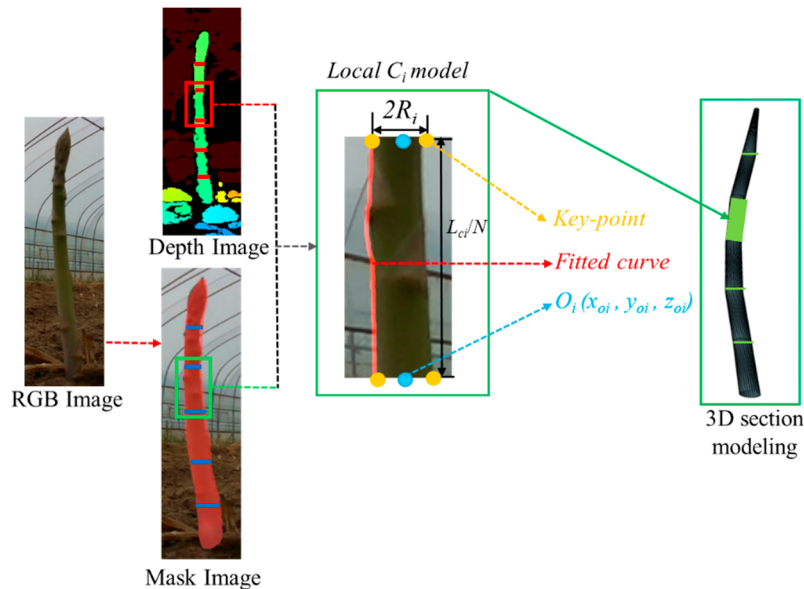


Figure 10. Schematic diagram for 3D section modeling of stems (e.g., 6 equal sections).

For example, when dividing a stem into N cylindrical sections, each cylinder C_i had a radius R_i and length L_i , represented as $\cup C_i(R_i, L_i)$. Given the stems' inclination and curvature, each L_i was calculated from fused depth data in the mask image, ensuring modeling accuracy. Specifically, the length L_i of green asparagus was derived through mask and depth images, coordinate transformation, and spatial line fitting, then averaged into N sections with each segment length L_{ci}/N . The radius R_i was similarly derived from the depth-fused mask. In camera space, the mask determined the bottom surface position of each C_i , with coordinates of both ends obtained from the bottom cutoff line in the mask image. Converting depth to camera coordinates gives world coordinates for each endpoint and a point on the cutoff line. Finally, C_i was fitted to find its center $O_i(x_{oi}, y_{oi}, z_{oi})$ and R_i in cross-section, accurately positioning and linking each cylinder.

The pseudocode for the section modeling of clustered green asparagus stems is presented in Algorithm 2. Firstly, the RGB-D sensor acquired the RGB image and the Depth image, which were stored as $RGBimg$ and $Depthimg$, respectively. Through the YS3AM proposed in this paper, target recognition, segmentation, and semantic information extraction were conducted on the $RGBimg$. The recognition boxes and masks were stored in $Boxes$ and $Maskimg$, respectively. Secondly, for each selected box $each$ in $Boxes$, the *SeparateAsparagus* function was constructed to separate each green asparagus in $Maskimg$. The *GetKeyPoint* function was constructed to extract the key point coordinates of the top, bottom, left, and right of each green asparagus. The *Calculate_L* function was constructed to calculate the length of the asparagus. Thirdly, the green asparagus was divided into N sections. For each section i , the bottom position $BottomPos$ of C_i was calculated. The *Calculate_R* and *GetCenterPoint* functions were, respectively, constructed to calculate the radius and center point of C_i based on each $BottomPos$. Finally, the *MapPostoCamere* function was constructed to convert the center point, length, and radius of C_i into camera coordinates (x, y, z) and plot C_i using the *PlotCylinder* function. This process was repeated until the modeling of the clustered green asparagus was accomplished.

Algorithm 2: 3D section of stem

```

1. Boxes, Maskimg ← YS3AM(RGBimg);
2. for each in Boxes do
3.     asp ← SeparateAsparagus(each, Maskimg);
4.     Top, Bottom, Left, Right ← GetKeyPoint(asp);
5.     L ← Calculate_L(asp, Depthimg);
6.     for i ← 1 to N do
7.         BottomPos ← L × (i - 1) / N + Bottom;
8.         R ← Calculate_R(asp, BottomPos, Depthimg);
9.         C ← GetCenterPoint(asp, BottomPos, Depthimg);
10.        x, y, z ← MapPostoCamera(C, R, L, Depthimg);
11.        PlotCylinder(x, y, z);
12.    end for
13. end for

```

2.6.2. Parameter Calculations of Section Modeling

(1) Length calculation of each section

To determine the length of the asparagus stem, this paper employed a scheme of fitting the outline curve of the asparagus stem. We first segmented the green asparagus within the prediction box using the SAM model. This segmentation allowed us to identify and isolate each individual asparagus stem, and obtain the contour of each green asparagus. Then, we addressed some missing pixels in the depth image using the method described in Section 2.5.1. This process ensured that we had a complete and accurate depth image. Scanning each pixel point on the contour, the 3D coordinates (x, y, z) of each pixel point in the camera coordinate system were calculated using the method outlined in Section 2.5.2, which provides a reliable way to transform the 2D pixel coordinates into their corresponding 3D spatial coordinates. Finally, to create a smooth and accurate representation of the asparagus stem, we fitted a spatial curve line to the pixel points on the contour. The spatial linear equation is fitted according to the least squares method:

$$\frac{x - x_0}{m} = \frac{y - y_0}{n} = \frac{z - z_0}{p} \quad (4)$$

where (x_0, y_0, z_0) is any point on the contour and (m, n, p) is the direction vector on the fitted line. An equivalent transformation of the above equation can be expressed as:

$$\begin{cases} x = \frac{m}{p}(z - z_0) + x_0 = k_1 z + b_1 \\ y = \frac{n}{p}(z - z_0) + y_0 = k_2 z + b_2 \end{cases} \quad (5)$$

where,

$$k_1 = \frac{m}{p}, b_1 = x_0 - \frac{m}{p}z_0, k_2 = \frac{n}{p}, b_2 = y_0 - \frac{n}{p}z_0 \quad (6)$$

Based on the principle of least squares fitting, the space curve equation fitted to the green asparagus can be expressed as:

$$\begin{cases} x = k_1 \times z + b_1 \\ y = k_2 \times z + b_2 \end{cases} \quad (7)$$

where,

$$k_1 = \frac{2 \sum_{i=1}^n x_i z_i - \sum_{i=1}^n x_i \times \sum_{i=1}^n z_i}{2 \sum_{i=1}^n z_i^2 - \sum_{i=1}^n z_i \times \sum_{i=1}^n z_i}, b_1 = \frac{\sum_{i=1}^n x_i - k_1 \sum_{i=1}^n z_i}{2},$$

$$k_2 = \frac{2 \sum_{i=1}^n y_i z_i - \sum_{i=1}^n y_i \times \sum_{i=1}^n z_i}{2 \sum_{i=1}^n z_i^2 - \sum_{i=1}^n z_i \times \sum_{i=1}^n z_i}, b_2 = \frac{\sum_{i=1}^n y_i - k_2 \sum_{i=1}^n z_i}{2}. \quad (8)$$

To determine the length of each approximate cylinder along the fitted line of the green asparagus stem, we need to start by identifying the top point and the bottom point of the stem section. Based on the idea of stem section, the fitted line connecting these two points was evenly divided into N sections. The length of each approximate cylinder section was the Euclidean distance between the endpoints of each section. For two spatial points $P_i(x_i, y_i, z_i)$ and $P_{i+1}(x_{i+1}, y_{i+1}, z_{i+1})$, the distance L_i is calculated as:

$$L_i = \sqrt{(x_i - x_{i-1})^2 + (y_i - y_{i-1})^2 + (z_i - z_{i-1})^2} \quad (9)$$

Since the sections were evenly divided, this distance would be approximately the same for each section; L_i could be considered the approximate length of the cylinder i . By using this method, we could determine the length of each section of the cylinder that approximates the green asparagus stem (Figure 11).

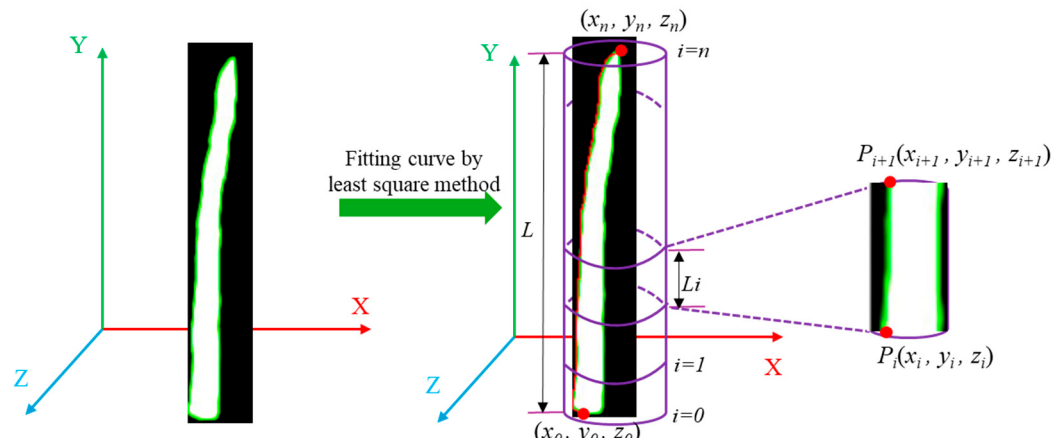


Figure 11. Calculating the length of each stem using the least square fitting curve.

(2) Center and diameter calculation of each section

Next, it was necessary to calculate the center and radius of the approximate cylinder for each section of the asparagus stem. In the camera coordinate system, we assumed that each section was parallel to the y -axis. We then made m horizontal cuts parallel to the xoz -plane (Figure 12b). Each cut revealed that the intersection of the horizontal section with the cylinder maintained a circular surface. Due to the camera's shooting angle, we only observed a portion of the arc of the circular surface at a time. To address this, we selected three points $P_{i1}(x_{i1}, z_{i1})$, $P_{i2}(x_{i2}, z_{i2})$, $P_{i3}(x_{i3}, z_{i3})$ on the circular arc of an intersecting circular surface (Figure 12c). Using these points, we determined the center $o'(x_{io}, z_{io})$ of the circle that the arc belonged to, as well as its radius (r). The specific calculation method is as follows:

$$x_{io} = \frac{ed - bf}{ad - bc} \quad (10)$$

$$z_{io} = \frac{ce - af}{bc - ad} \quad (11)$$

$$\begin{aligned} r &= \sqrt{(x_{io} - x_{i1})^2 + (z_{io} - z_{i1})^2} \\ &= \sqrt{\left(\frac{bf - de}{bc - ad} - x_{i1}\right)^2 + \left(\frac{ce - af}{bc - ad} - z_{i1}\right)^2} \end{aligned} \quad (12)$$

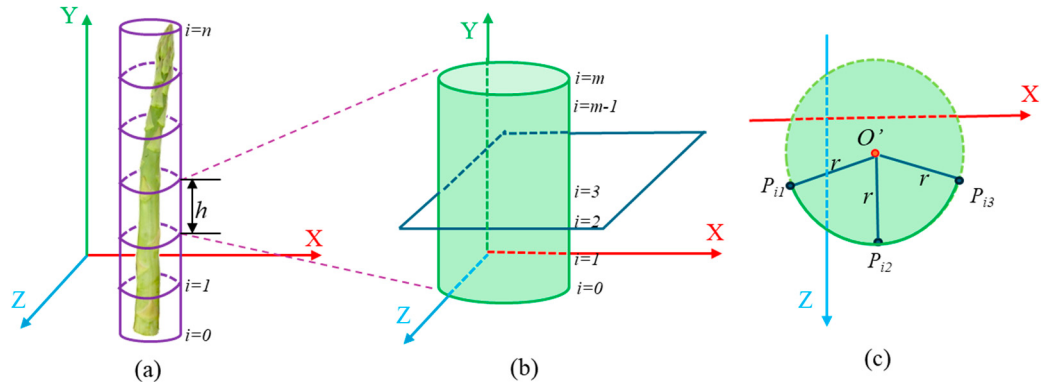


Figure 12. Calculating the width of each stem. (a) The approximate cylinder enclosing the stem of the asparagus stem. (b) A section of cylinder. (c) The intersecting circular surface.

In Equations (6)–(8),

$$\left\{ \begin{array}{l} a = x_{i1} - x_{i2} \\ b = z_{i1} - z_{i2} \\ c = x_{i1} - x_{i3} \\ d = z_{i1} - z_{i3} \\ e = \frac{x_{i1}^2 - x_{i2}^2 + z_{i1}^2 - z_{i2}^2}{2} \\ f = \frac{x_{i1}^2 - x_{i3}^2 + z_{i1}^2 - z_{i3}^2}{2} \end{array} \right. \quad (13)$$

Based on the above equations, we could then construct the binary function on the radius (r), defined as:

$$f(r) = \sqrt{\left(\frac{bf - de}{bc - ad} - x_{i1}\right)^2 + \left(\frac{ce - af}{bc - ad} - z_{i1}\right)^2} \quad (14)$$

From the definition of the limit of a binary function, all points $P_i(x_i, z_i)$ on the visible arc should satisfy:

$$|f(x_i, z_i) - A| < \varepsilon \quad (15)$$

where ε represents a given positive number, so A is the limit of when $P_i \rightarrow o'(x_{io}, z_{io})$. Specifically, A corresponds to the radius (r) of the circle in which the arc lies and $o'(x_{io}, z_{io})$ is the center of the circle. After these calculations, we were able to determine the base circle (center: $o'(x_{io}, z_{io})$ and radius: r) and length of each stem section.

2.6.3. Section Modeling Accuracy Assessment Methods

The differences in the thickness and inclination angle of the stem will inevitably cause differences in the accuracy of section modeling. The accuracy of 3D modeling is usually measured by the RMSE (Root Mean Square Error) index, which is a commonly used indicator to measure the accuracy of prediction models. It is used to measure the degree of difference between the predicted value and the actual observed value, i.e.,

$$RMSE = \sqrt{\sum_{i=1}^n (\hat{\eta}_i - \eta_i)^2 / n} \quad (16)$$

where $\hat{\eta}_i$ is a point on the section cylinder, η_i is the real measured value of a point on the shoot, and n is the number of samples. For the section number N , the RMSE index is statistically calculated for each section, and RMSE_i is the index value of section C_i . The maximum value of RMSE is taken as the indicator of the modeling accuracy of the entire green asparagus stem, i.e., $\text{MAX}(\text{RMSE}_i)$.

When computing the RMSE_i of the C_i section, theoretically, it is necessary to perform calculations for all points in space and those on the section cylindrical surface. However, this approach would reduce computational efficiency and is unnecessary, as RGB-D sensors can only collect depth information from one side, leaving the back of the asparagus stem invisible. Thus, it is impossible to obtain the complete 3D information of the asparagus stem, and it is also infeasible to take all points as the basis for calculating RMSE. Analyses reveal that assuming the cross-section of the green asparagus is circular, using the maximum offset as an indicator, the offset of the stem can be replaced by the axis offset. Therefore, finding the $\text{MAX}(\text{RMSE}_i)$ is equivalent to determining the offset of the cross-sectional center. We accelerated the calculation of the RMSE_i index for each C_i section by using a small number of typical values instead of all points. These points consisted of the centers of the cross-sections passing through specific positions on the stem, including the extreme points on the depth map and the inflection points on the contour of the mask image.

The pseudocode in Algorithm 3 illustrates the process for computing modeling indices of each green asparagus section. Correspondingly, the RGB image (RGBImg) and depth image (DepthImg) were acquired from the RGB-D sensor. Semantic extraction of RGBImg was performed using the YS3AM framework proposed in this paper, with masks subsequently stored in MaskImg . The sequences for KeyPoints and ModelPoints were initialized accordingly. To identify all extreme points within MaskImg and DepthImg , a function named *findExtremePoints* was developed to store these points in SpecialPoints . Additionally, two functions—*CalculateCenter* and *MapModelCenter*—were constructed to compute both the true cross-sectional centers and their corresponding model cross-sectional centers mapped to identical positions. And these results were recorded in KeyPoints and ModelPoints , respectively. Following this, RMSE_{C_i} was then calculated by iterating over variable points, with the maximum RMSE across sections serving as the overall evaluation index for the asparagus stem.

Algorithm 3: The computation of accuracy metrics

1. $\text{MaskImg} \leftarrow \text{YS3AM}(\text{RGBImg})$;
 2. $\text{KeyPoints} \leftarrow []$;
 3. $\text{ModelPoints} \leftarrow []$;
 4. $\text{RMSE}_{\text{C}_i} \leftarrow 0$;
 5. **for** each pixel in MaskImg and DepthImg **do**
 6. $\text{SpecialPoints} \leftarrow \text{findExtremePoints}(\text{MaskImg}, \text{DepthImg})$;
 7. $\text{KeyPoints} \leftarrow \text{CalculateCenter}(\text{SpecialPoints})$;
 8. $\text{ModelPoints} \leftarrow \text{MapModelCenter}(\text{SpecialPoints})$;
 9. **end for**
 10. **for** each $Kpoint$ in KeyPoints and $Ppoint$ in ModelPoints **do**
 11. $\text{RMSE}_{\text{C}_i} \leftarrow \text{RMSE}_{\text{C}_i} + \text{sqrt}((Kpoint - Ppoint)^2)$;
 12. **end for**
 13. $\text{RMSE}_{\text{C}_i} \leftarrow \text{RMSE}_{\text{C}_i} / \text{Sizeof}(\text{KeyPoints})$;
 14. **return** RMSE_{C_i} ;
-

2.6.4. Calculation of the Section Count for Adaptive Modeling

Variations in length, thickness, and posture among asparagus stems lead to differences in modeling accuracy when a fixed number of sections N is used uniformly. However,

accurate and consistent modeling across all stems is essential for subsequent path planning and end-effector motion control. Therefore, selecting an appropriate number of sections for each stem is crucial. This paper introduced an adaptive-section modeling methodology focused on clustered green asparagus stems based on stem length. Specifically, it involved automatically selecting the number of sections according to stem lengths to ensure consistent modeling accuracy for all stems within the camera's field of view. Assuming that the length of an intact stem was L and defining parameter n as the section count, we outlined expectations for different stems as follows:

$$N = \underset{n}{\operatorname{Argmin}}(P(C_s, A_s) \leq \varepsilon) \quad (17)$$

where P denotes the model accuracy evaluation function, and $C_s = \cup C_i (R_i, L_i)$ represents the N -section model. A_s refers to the artificially collected empirical data, and ε signifies the allowable accuracy. Assuming that the positioning accuracy of the actuator was not considered, ε could be derived from the measurement precision of the RGB-D sensor. During practical measurements, due to the irregular surface of stems, the depth measurement error of the RGB-D sensor under illuminated conditions was 5 mm. Thus, ε could be approximated as $\varepsilon = 5 \times 10^{-3}$. It was evident that n should be a function of asparagus stem length L . An increase in n correlated with enhanced modeling accuracy and greater model fidelity. However, a larger value for n also resulted in increased computational complexity. Therefore, for different asparagus stems i and j , there should be:

$$P(C_{n_i}, A_i) = P(C_{n_j}, A_j) \leq \varepsilon \quad (18)$$

where $i, j \in N$. The result of the function P determined the accuracy of the visual model of green asparagus, depending on the calculated values of the evaluation indicators in Section 2.6.3.

The pseudocode for calculating the adaptive modeling section count of asparagus stems is provided in Algorithm 4. An iterative methodology was employed to ascertain the optimal number of sections. For green asparagus i , $\varepsilon = 5 \times 10^{-3}$ was initialized as the termination criterion for iteration, and the initial section count was set to N (this paper began with $N = 4$). The *CalculateP* function was developed to compute the RMSE value of 3D modeling when the section count was equal to 4, followed by an assessment of whether the modeling accuracy requirements were satisfied. If not, an iterative loop commenced wherein the section count was incremented by one until satisfactory modeling accuracy was achieved. The resultant section count represented the optimal segmentation that met the specified accuracy criteria.

Algorithm 4: Calculating the number of sections

1. $\varepsilon \leftarrow 5 \times 10^{-3}$;
 2. $n_i \leftarrow N$;
 3. $\text{RMSE} \leftarrow \text{CalculateP}(C_{n_i}, n_i)$;
 4. **while** $\text{RMSE} \geq \varepsilon$ **do**
 5. **if** $n_i > N_{\max}$ **then**
 6. **break**;
 7. **end if**
 8. $n_i \leftarrow N + 1$;
 9. $\text{RMSE} \leftarrow \text{CalculateP}(C_{n_i}, n_i)$;
 10. **end while**
 11. **return** n_i ;
-

3. Experimental Results

The multi-task network in YS3AM was a cascade of two networks, prediction box detection and mask segmentation. During prediction, these networks were interconnected in a head-to-tail configuration, resulting in an output that delineates the contour of asparagus stems within the full image. Therefore, both the structure of the network and its combination had an influence on the final visualization of the spatial location of each green asparagus. Comparative experiments were designed to select the best combination of networks. This encompassed the presentation of model recognition and segmentation results, ablation experiments assessing the detection accuracy of green asparagus using various improvement strategies. Furthermore, this paper validated the accuracy of the proposed adaptive spatial segmentation model for green asparagus. These included evaluations of key-point offset testing, measurements of stem length and width errors, and Laboratory Farm random stalk assessment.

The detection network in this paper was implemented using the Pytorch framework; the specific hardware configuration and experimental setup are detailed in the following Table 2.

Table 2. Hardware configuration and experimental environment.

Hardware	Configuration	Environment	Version
OS	Windows11	Python	3.8
CPU	Intel(R) Core (TM) i9-12900H @2.50GHz	PyTorch	1.12
GPU	GeForce RTX 3060(6G)	PyCharm	2022.3.1
RAM	16G	CUDA	11.6
HardDisk	1T	cuDNN	8.8.0

3.1. Evaluation Metrics

The YOLOv7 of YS3AM model was initialized with pre-trained weights from the COCO dataset and fine-tuned on our custom dataset. All hyperparameters were selected according to the official configuration. The optimizer used was Adaptive Moment Estimation (Adam), with the momentum coefficient and weight decay coefficient set to the default values of 0.937 and 0.0005, respectively. The learning rate was set to 0.005, and the image resolution was normalized to 640×640 . Due to limitations in GPU memory and the number of CPU cores, the batch size was set to 8, the number of workers was set to 4, and the training was conducted for 200 epochs.

This paper evaluated the performance of each group by comparing the precision, recall, F1 score, loss function, and detection time. Specifically, the *Precision* was defined as the ratio of the number of correct identifications of green asparagus on the image to the total number. The *Recall* was the proportion of correctly detected green asparagus to all green asparagus that should be detected. The *F1* score was the harmonic mean of *Precision* and *Recall*, and it provided a balanced evaluation of a model's performance. Additionally, the number of parameters represented the total count of parameters. The gradient was the maximum rate of change of the function along the gradient direction. GFLOPs represented the number of floating-point operations required for model inference.

This paper utilized binocular stereo vision technology to perform the localization and segmentation of clustered green asparagus, while also developing a 3D model for adaptive section based on stem length. Inevitably, discrepancies arise between the actual positions of outdoor crops and their predicted locations, leading to deviations in the constructed visualization model from real-world conditions. Consequently, when assessing the green

asparagus model, evaluation metrics such as the coefficient of determination (R^2), root mean square error (RMSE), and Pearson's correlation coefficient were recommended.

3.2. Model Performance Test

3.2.1. Detection and Segmentation Results

YS3AM could identify green asparagus under conditions of light variation, complex backgrounds, and interwoven overlaps, showing good recognition and segmentation results. In this section, we validate the recognition results of YS3AM using the Sunny and Cloudy datasets, as well as the total dataset of all images, following the method described in Section 2.4. Table 3 presents the detection results for the total dataset, including various metrics (Precision, Recall, F1, and mAP) at different confidence levels, and the black data indicates optimal results. Figure 13 illustrated a comparison of the various mAP and loss obtained by all models trained with images from the Sunny, Cloudy, and Total datasets ($\text{IoU} = 0.2$, $\text{Conf} = 0.6$). It could be observed that the mAP value (0.972) using the Total training set images was slightly higher than that of Sunny (0.966) and Cloudy (0.961). The box-loss (0.036) for the Total dataset images was higher than for Sunny (0.024) and Cloudy (0.028). The overall model performance was stable, with the obj-loss (0.068) being slightly higher than that of Sunny (0.021) and Cloudy (0.024), and the mIOU (0.874) was lower than Sunny (0.913) and Cloudy (0.900). After comparison, the overall performance of YS3AM was stable.

Table 3. Detection results of the total dataset for different confidence levels (IoU threshold set to 0.2).

Conf	Precision (%)	Recall (%)	F1	mAP (%)
0.5	98.35%	95.14%	0.967	96.84%
0.6	98.75%	95.46%	0.971	97.16%
0.7	98.36%	95.31%	0.968	96.77%
0.8	97.76%	95.54%	0.966	97.07%
0.9	98.44%	95.54%	0.969	96.89%

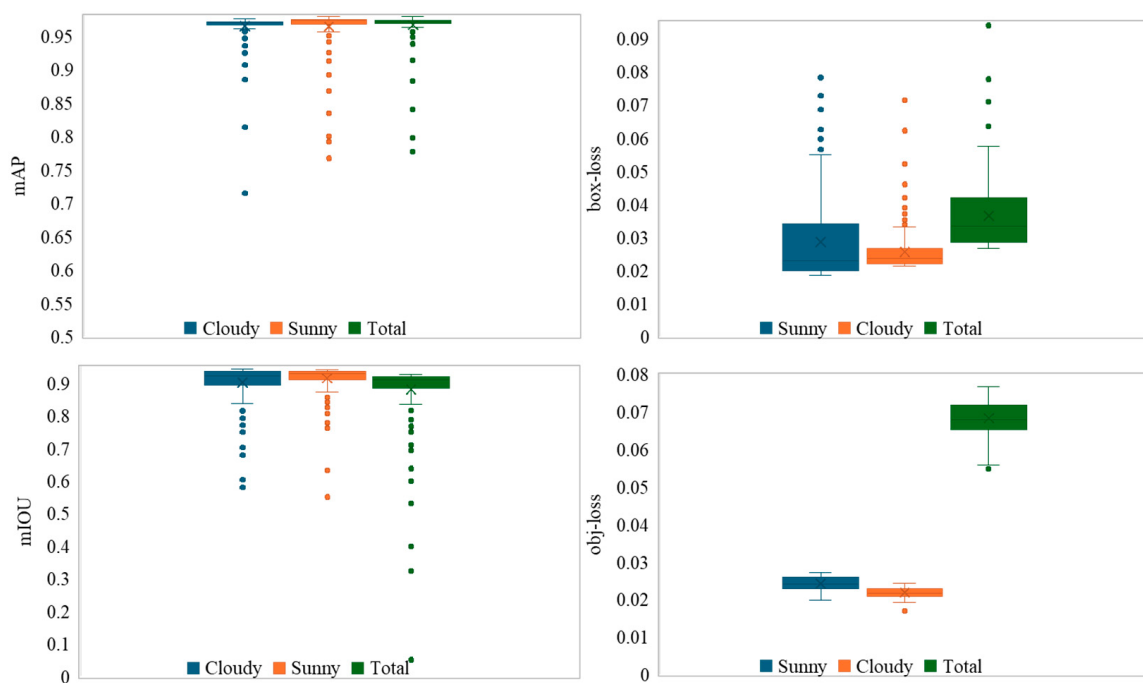


Figure 13. Evaluation metrics for models on the three datasets.

However, the overall metrics showed that the detection performance on the Sunny dataset was superior to that on the Cloudy dataset. Binocular stereo vision methods rely on natural light in the environment to capture images and are very sensitive to ambient lighting conditions. Due to the influence of environmental factors such as changes in light angle and light intensity, the brightness difference between two images captured by the depth camera is relatively large, which presents a considerable challenge for matching algorithms. The mAP detection rate for the Sunny dataset was 14.29% higher than that for the Cloudy dataset, the box-loss detection rate was 16.67% higher, the obj-loss detection rate was 2.52% lower, and the mIOU was 1.42% higher. Figure 14 illustrated the recognition and segmentation effect of our model on clustered green asparagus under different lighting conditions, such as dense, overlapping and occlusion conditions, and the detection and segmentation accuracies of the model were high.

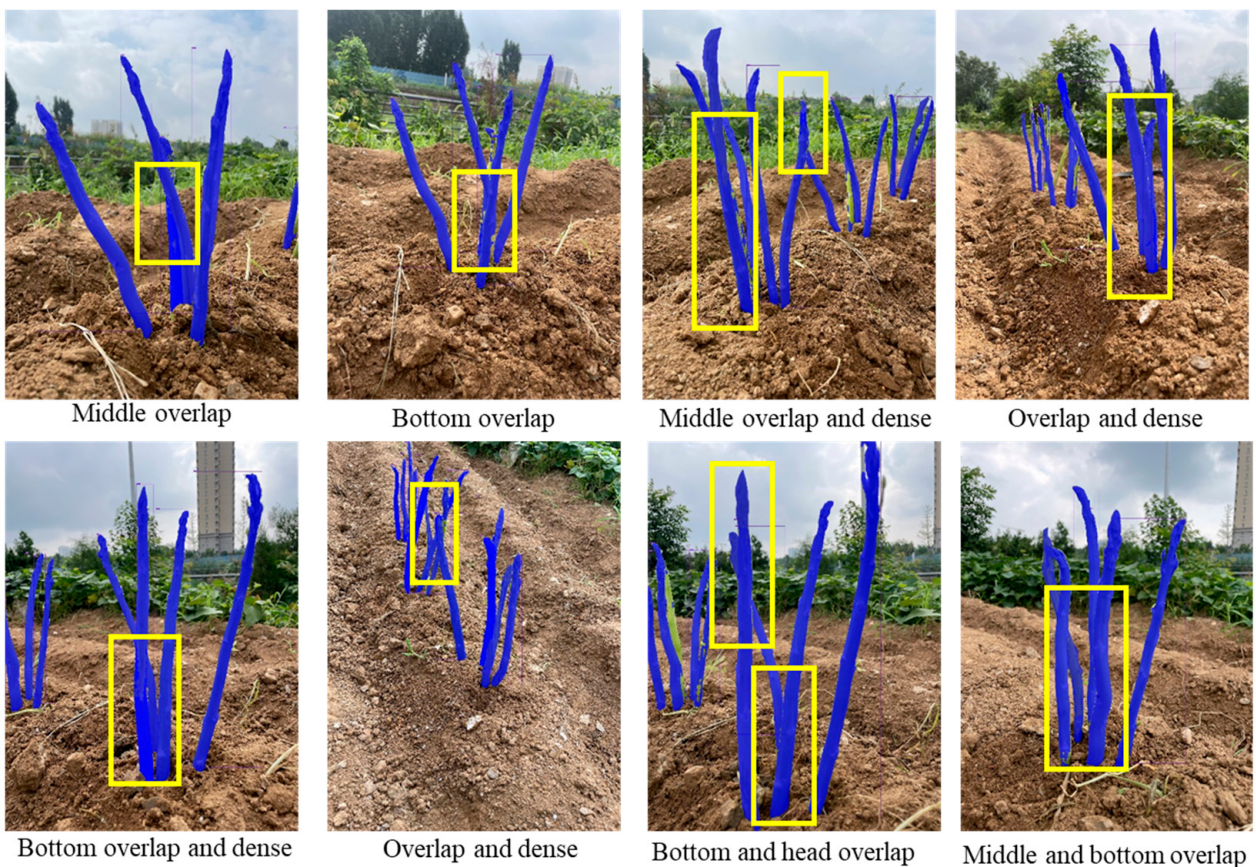


Figure 14. Detection and segmentation result of green asparagus. The overlaps of asparagus stem are marked with yellow boxes.

3.2.2. The Results of Ablation Studies

As previously mentioned, we made four main improvements to the original YOLOv7, including some structural changes to the network (e.g., lightweight CBH-S module, MobileOne ultra-lightweight module for obtaining a larger receptive field at different scales, lightweight down-sampling module (CAConv) that focused on location information, shallow-to-deep cross-scale fusion architecture). Therefore, we further performed ablation experiments to determine which modification contributed the most to the proposed YS3AM network, which led to better detection capability in this work. Model A represented the original YOLOv7 model, while models B to J represented varying degrees of improvement to model A under the most optimal hyperparameters. Model B implemented a lightweight model that replaced the CBS module with the CBH-S

module. Model C implemented a lightweight MobileOne replacing the ELAN module of the YOLOv7 backbone. Model D implemented the use of lightweight CAConv modules that combined locational information and attention mechanisms to replace the MPCConv module in the Neck section. Model E achieved multi-feature extraction from deep to shallow layers through cross-scale fusion. Model F was the fusion of models B and C, achieving multi-level feature extraction based on lightweight. Model G was the fusion of models B, C, and D, achieving multi-path information fusion while being lightweight. Model H was the fusion of models B, C, and E, achieving lightweight cross-scale fusion. Model I was the fusion of models B, D, and E, achieving multi-information fusion across scales. Model J was the improved model proposed by us. Table 4 shows the results of the ablation study, which clearly indicates that these four structural improvements are beneficial to the performance of YS3AM. The black data indicates optimal results. As expected, YS3AM performed the best in the ablation study because it combined structural and attention modifications.

Table 4. The ablation experiment results.

Model	CBH-S	MobileOne	CAConv	Cross-Scale Fusion	Precision (%)	Recall (%)	mAP (%)	Final Loss	F1 (%)	Detection Time Per Image (ms)	GFLOPs
A					97.79	93.98	95.96	0.062	95.85	14.9	105.1
B	★				98.42	95.69	97.45	0.031	97.04	13.2	103.2
C		★			98.05	93.34	96.71	0.059	95.64	16	43
D			★		98.19	94.25	96.71	0.059	96.18	14.7	55.1
E				★	98.32	95.68	97.82	0.030	96.98	95.6	104.8
F	★	★			98.00	94.19	97.36	0.061	96.06	14.9	47.9
G	★	★	★		98.41	93.42	96.56	0.061	95.85	14.1	50.7
H	★	★		★	98.64	93.64	96.58	0.060	96.07	12.8	42.9
I	★		★	★	98.25	93.95	96.43	0.059	96.05	13	53
J	★	★	★	★	98.58	95.61	97.76	0.030	97.07	12	50.8

As shown in Table 3 and Figure 15, the Precision of the YS3AM model is the highest, while the YS3AM model achieved the highest Precision. Although the Recall of the model was 0.07 percentage points lower than Model E, the F1 score remained superior to other models. The mAP of the YS3AM model was marginally lower than that of Model E, which suggested that cross-scale fusion methods could adequately capture the complex target in the model down-sampling process (e.g., stem interlacing) features. The cross-scale fusion strategy provided a more comprehensive understanding of the data. Replacing CBS with CBH-S further improved the metrics, and the total Loss of the model was reduced by 50.65%, reflecting the stronger generalization ability of the lightweight module. With the different modules introduced in YOLOv7, there was a relatively significant and proportional decrease in the computation of the model, especially with Model H being the lowest. This also illustrated the substantial contribution of lightweight structures to our model. Therefore, although all the above models were based on the YOLO architecture and had achieved good results in some cases, they were not generalizable and require special algorithms to be designed for different datasets and practical needs. The effectiveness of the YS3AM model in recognizing green asparagus growing in clusters outdoors was verified by comparing it with the above models.

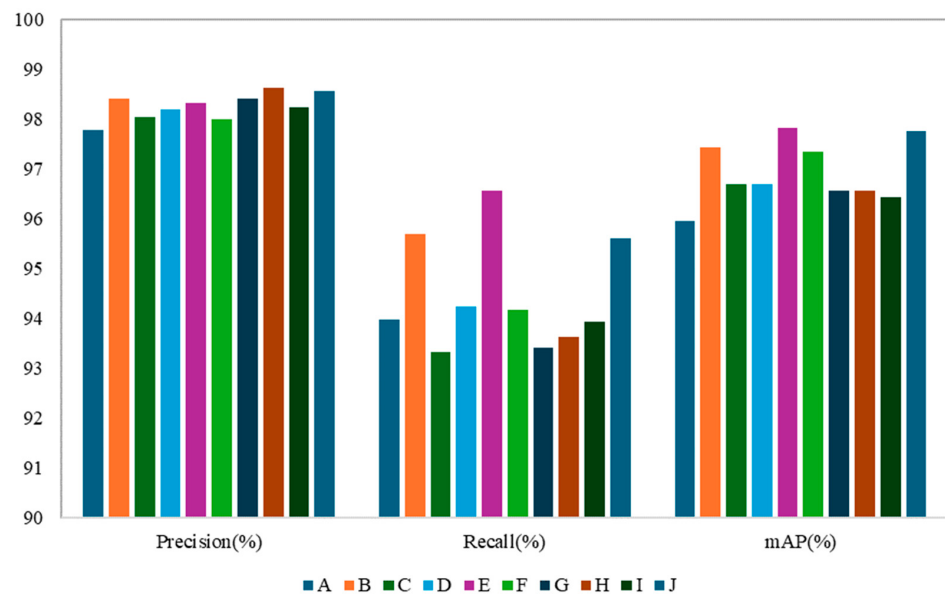


Figure 15. Results of evaluation indicators for different models.

3.3. Assessment of Spatial Information Visualization in Green Asparagus

3.3.1. Key-Point Deviation Detection Test Results

An experiment was performed in a laboratory environment to determine the optimal number of sections for the visualization model. Four sets of 12 green asparagus (Figure 16) were used as targets for this test. The length standard for harvesting the stems of green asparagus varies according to the purpose. If used as raw materials for processing, the harvest is carried out when the stems reach a length of 14~21 cm. For domestic market sales, a length of 25~28 cm is appropriate. And for the winter market in the northern regions, the length of the asparagus stems is about 30~35 cm. Therefore, the length intervals we select are as follows: 15~20 cm, 21~25 cm, 26~30 cm, and 31~35 cm.

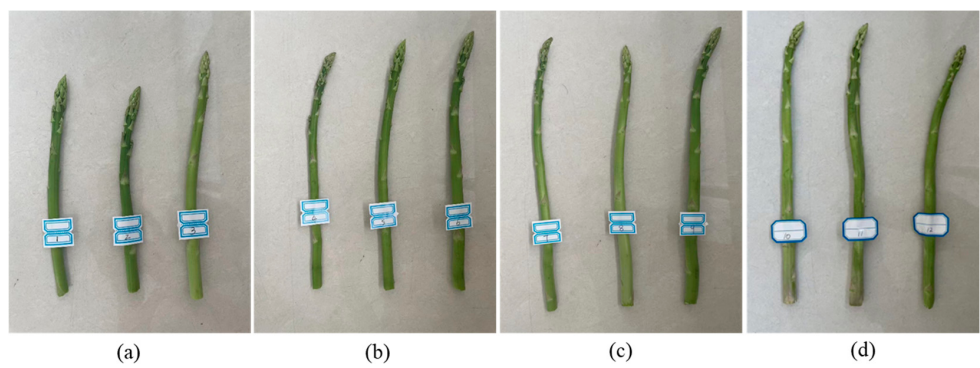


Figure 16. Targets used for the key-point test. (a) 15~20 cm, (b) 21~25 cm, (c) 26~30 cm, (d) 31~35 cm.

The targets were fixed in a vertical position. The camera was mounted on a tripod about 35–40 cm from the test targets (Figure 17). In this paper, a section testing approach was adopted. Each green asparagus was equally divided into 4, 6, 8, and 10 sections, respectively, and each section of the asparagus stem could be approximated as a cylinder. Furthermore, we selected certain key points on the edge of the bottom surface of each cylinder (including the leftmost, center, and rightmost points), and calculated the average RMSE of the predicted and point cloud true depths of each key point in different section methods in accordance with the precision evaluation method in Section 2.6.3. All RMSE results of the key-point test are summarized in Table 5, and the black data indicates optimal results. The section model is shown in Figure 18.

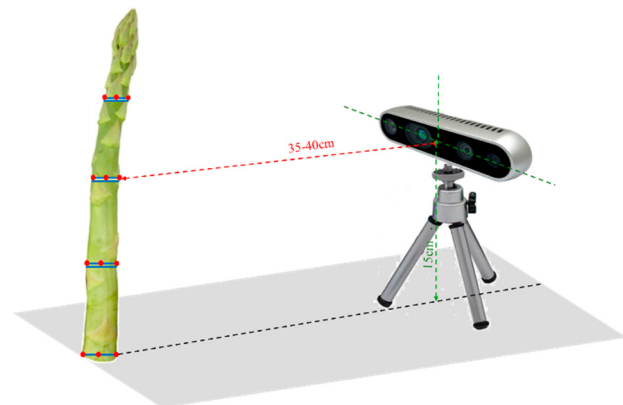


Figure 17. Key_Point test.

Table 5. The RMSE results of key point location deviation.

		4-Section	6-Section	8-Section	10-Section
Group 1	1	0.00307	0.00299	0.0028	0.00206
	2	0.00481	0.00461	0.00171	0.00296
	3	0.00468	0.00611	0.00662	0.00621
Group 2	4	0.00258	0.00301	0.00279	0.00288
	5	0.00523	0.00389	0.00299	0.00303
	6	0.000763	0.00444	0.00659	0.00374
Group 3	7	0.00354	0.00281	0.00419	0.00274
	8	0.01299	0.01358	0.00261	0.00177
	9	0.01646	0.05857	0.01982	0.00322
Group 4	10	0.01053	0.00751	0.01128	0.00347
	11	0.00318	0.00392	0.00216	0.00397
	12	0.00248	0.00293	0.00252	0.00313

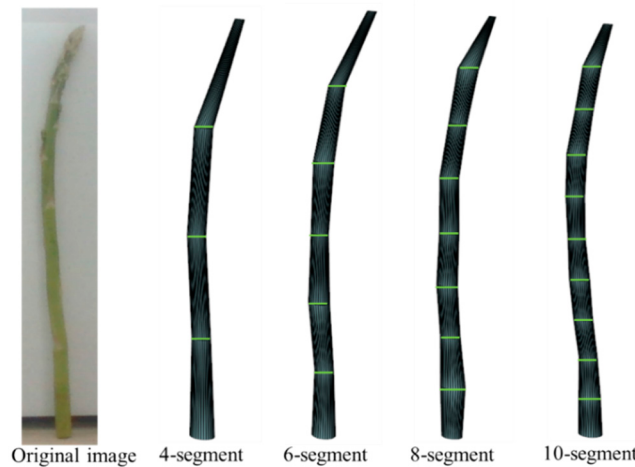


Figure 18. Examples of different 3D section models.

As can be seen by comparing Table 5, when exploring the optimal number of sections, both the MAX(RMSE_i) and the limit of the maximum error needed to be taken into consideration. Firstly, for the three green asparagus stems with lengths ranging from 15 to 20 cm, the MAX(RMSE_i) existed when No. 1 and No. 2 were equally divided into 4 sections; for No. 3, the MAX(RMSE_i) existed when it was equally divided into 8 sections. Since the maximum error should not exceed $\varepsilon = 5 \times 10^{-3}$ during the optimal section, the accuracy of No. 3 was the highest when it was equally divided into 4 sections. Then, observing the RMSE results of the three green asparagus stems with lengths ranging from 21 to 25 cm,

the visualization model had the highest accuracy when No. 4 was equally divided into 6 sections; for No. 5, although the MAX(RMSE_i) existed when it was equally divided into 4 sections, it obviously exceeded the maximum error, and thus, it was most appropriate to equally divide it into 6 sections; the situation of No. 6 was the same as that of No. 5, and finally, it was most suitable to equally divide it into 6 sections. Next, for the three green asparagus stems with lengths ranging from 26 to 30 cm, the MAX(RMSE_i) of No. 7 occurred when it was equally divided into 8 sections and did not exceed the maximum error; for No. 8 and No. 9, the MAX(RMSE_i) occurred when they were equally divided into 6 sections, but due to the limit of the maximum error, the accuracy was the highest when they were equally divided into 8 sections. Finally, observing the three green asparagus stems with lengths ranging from 31 to 35 cm, when No. 10 was equally divided into 8 sections, it exceeded the maximum error, and thus, equally dividing it into 10 sections was the best choice; both No. 11 and No. 12 had the MAX(RMSE_i) when equally divided into 10 sections and did not exceed the maximum error. The above 12 green asparagus stems could fully cover the length requirements of suitable harvestable green asparagus for different application needs. Therefore, a conclusion could be drawn. That conclusion was that green asparagus with lengths ranging from 15 to 20 cm could be equally divided into 4 sections; those with lengths ranging from 21 to 25 cm could be equally divided into 6 sections; green asparagus with lengths ranging from 26 to 30 cm could be equally divided into 6 or 8 sections; and those with lengths ranging from 31 to 35 cm could be equally divided into 8 or 10 sections.

3.3.2. The Length and Width Measurement Results

Through visits and investigations of multiple planting parks, mature green asparagus stems typically present an upright state, with a smooth and straight surface. Hence, apart from considering the deviation degree of some key points at the section parts of the asparagus stems, we can also conduct evaluations by judging the errors in the length and width of the stems. The 12 green asparagus stems in Section 3.3.1 were still subject to testing. All errors of the length test and width test are summarized in Tables 6 and 7, also shown in Figures 19 and 20 for better comprehension.

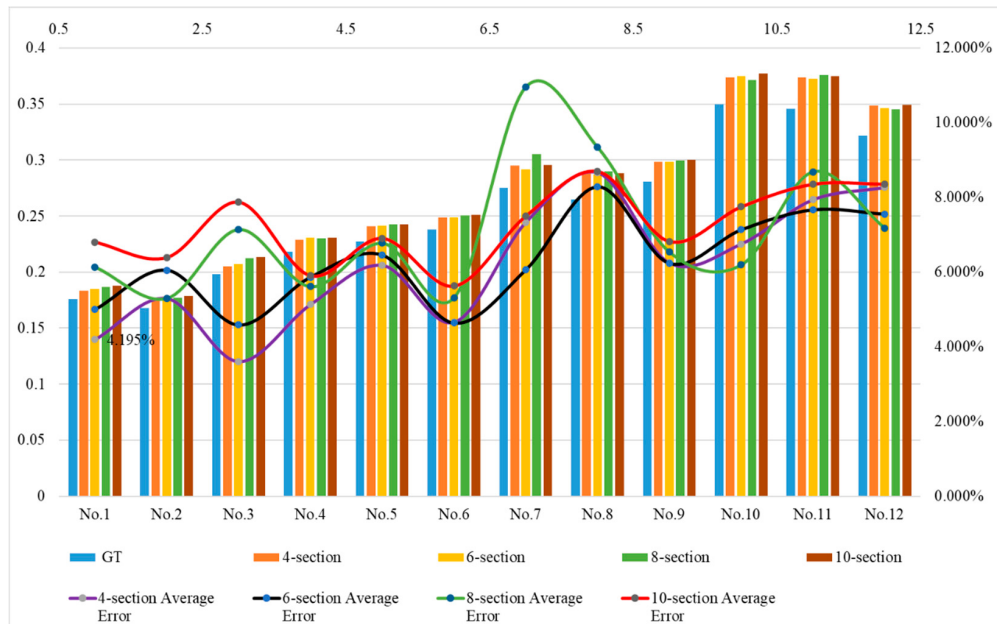
Table 6. Length analysis for different sections of table (unit: m).

		4-Section			6-Section			8-Section		10-Section	
		GT (m)	YS3AM (m)	Error (%)	YS3AM (m)	Error (%)	YS3AM (m)	Error (%)	YS3AM (m)	Error (%)	
Group 1	1	0.176	0.183	4.195	0.185	5.000	0.187	6.136	0.188	6.806	
	2	0.168	0.177	5.296	0.178	6.054	0.177	5.297	0.179	6.396	
	3	0.198	0.205	3.607	0.207	4.584	0.212	7.140	0.214	7.878	
Group 2	4	0.218	0.229	5.131	0.231	5.865	0.230	5.610	0.231	5.908	
	5	0.227	0.241	6.183	0.242	6.456	0.242	6.774	0.243	6.908	
	6	0.238	0.249	4.659	0.249	4.636	0.251	5.317	0.251	5.628	
Group 3	7	0.275	0.295	7.335	0.292	6.065	0.305	10.958	0.296	7.506	
	8	0.265	0.288	8.662	0.287	8.285	0.290	9.339	0.288	8.701	
	9	0.281	0.299	6.245	0.299	6.234	0.299	6.536	0.300	6.823	
Group 4	10	0.35	0.374	6.755	0.375	7.136	0.372	6.192	0.377	7.754	
	11	0.346	0.373	7.940	0.373	7.670	0.376	8.686	0.375	8.358	
	12	0.322	0.349	8.267	0.346	7.552	0.345	7.180	0.349	8.360	

Abbreviations: GT (Ground True): actual ground measured length of point cloud. YS3AM: indicates the length of model testing. Error: error rate of model and manual measurement error.

Table 7. Width analysis for different sections of table (unit: mm).

NO	4-Section				6-Section				8-Section				10-Section			
	Mean (GT)	Mean (Model)	Error Std (%)	Mean Error (%)	Mean (GT)	Mean (Model)	Error Std (%)	Mean Error (%)	Mean (GT)	Mean (Model)	Error Std (%)	Mean Error (%)	Mean (GT)	Mean (Model)	Error Std (%)	Mean Error (%)
1	9.208	9.524	0.251	3.223	8.697	9.307	0.581	5.860	8.716	9.531	1.318	6.906	8.904	9.418	0.622	10.458
2	8.623	9.29	0.787	7.261	8.310	9.308	1.040	10.718	8.305	9.211	0.735	9.838	8.375	9.125	0.751	8.220
3	8.830	8.892	0.621	0.699	8.852	9.466	0.966	6.486	9.013	9.256	0.727	2.625	8.753	8.841	0.545	0.998
4	7.852	7.963	0.136	1.420	7.938	8.016	0.313	0.981	7.929	8.14	0.835	2.663	7.860	8.163	0.395	3.851
5	9.288	9.691	0.022	2.440	9.350	9.832	0.234	3.209	9.33	9.563	0.432	4.166	9.032	10.832	0.678	16.619
6	9.170	9.289	0.719	1.280	9.106	9.095	0.591	2.084	9.231	9.182	0.388	0.539	9.151	8.986	0.595	0.481
7	8.200	5.209	0.360	2.234	8.365	8.182	0.741	0.109	8.394	8.346	0.688	0.580	8.156	8.403	0.574	2.932
8	9.520	10.719	1.421	11.187	9.048	9.848	0.588	12.278	9.894	11.108	0.835	8.585	9.319	10.594	1.233	10.928
9	9.274	10.064	1.417	7.872	9.183	9.455	0.196	2.886	9.388	10.42	0.861	6.927	9.387	10.116	0.838	5.130
10	12.958	13.784	1.017	6.069	13.031	13.487	1.180	3.380	13.074	13.487	1.070	3.067	12.931	13.297	0.579	2.754
11	14.783	15.631	0.971	5.428	14.503	15.996	1.043	9.331	14.313	15.406	0.999	7.091	14.938	15.774	0.687	5.301
12	12.989	14.692	1.275	11.589	12.853	14.745	1.620	12.835	12.93	14.46	1.795	10.582	13.002	14.191	2.304	8.381

**Figure 19.** Length measurement result.

As can be seen by comparing Table 6 (The black data indicated optimal results.), the length error of the first group of tests was the smallest when divided into 4 equal sections, that of the second group was the smallest when divided into 4 and 6 equal sections, that of the third group was the smallest when divided into 6 equal sections, and that of the fourth group was the smallest when divided into 6 and 8 equal sections. Combining the results of Section 3.3.1, we discovered that shorter green asparagus could attain higher accuracy with a smaller number of sections. However, for longer green asparagus, a greater number of sections did not necessarily imply higher model accuracy. On the contrary, a larger computational volume would excessively occupy system resources. This result was approximately the same as that of Section 3.3.1.

As can be seen by comparing Table 7 (The black data indicated optimal results.), the first row indicates the number of sections of each green asparagus. In the second row, Mean (GT) and Mean (Model), respectively, denote the average width measured manually and the average width measured by the model test, and Error Std represents the standard deviation of the error between the two measurement methods. Mean Error represents the ratio of the error between the two measurement results to the true width. By comparing the results from Figure 20a–h, the width error of green asparagus ranged between 0.45% and 16%, and the larger the width of the asparagus stem, the greater the error.

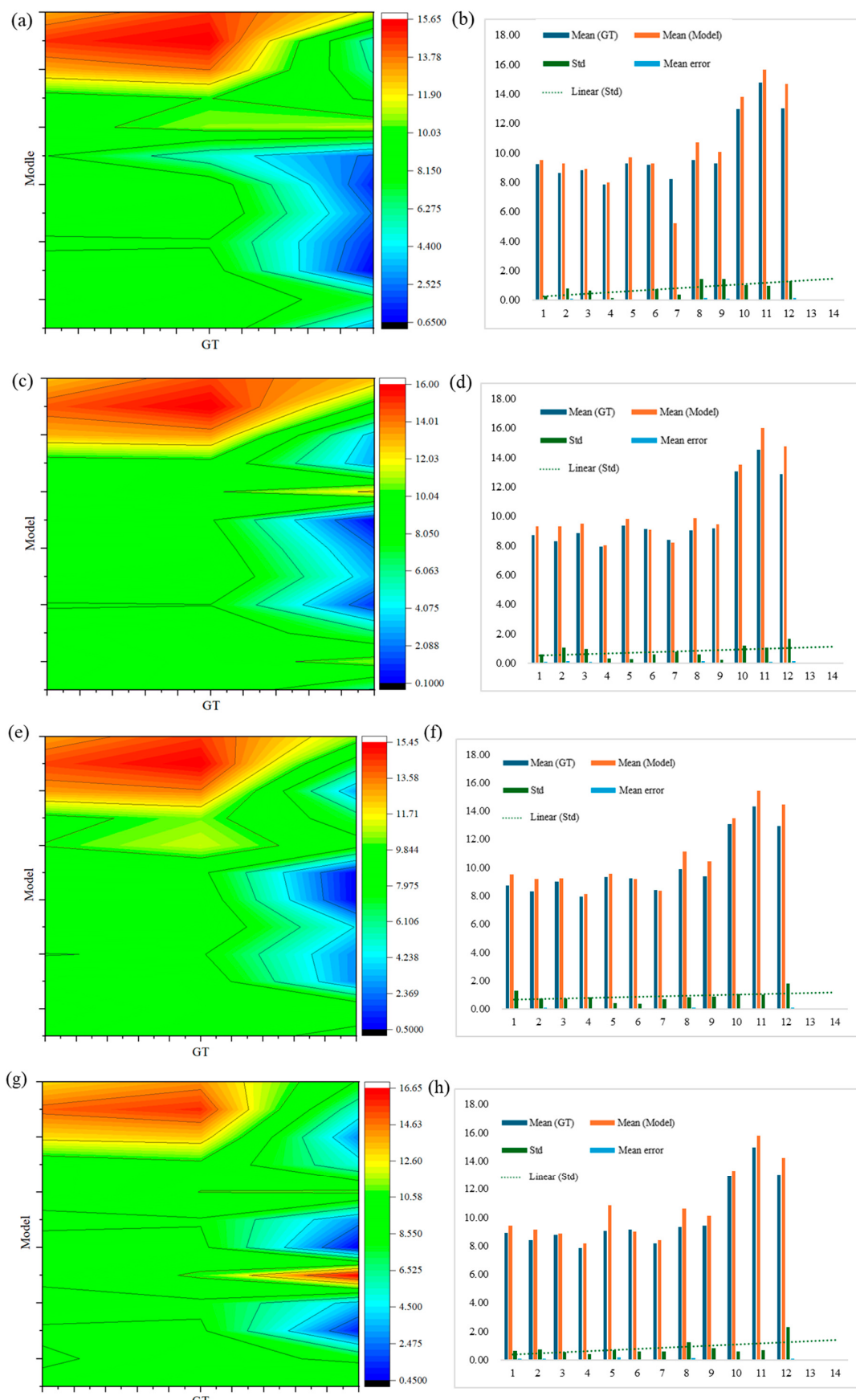


Figure 20. Width measurement result. **(a,b)** indicate the width error of 4-Section. **(c,d)** indicate the width error of 6-Section. **(e,f)** indicate the width error of 8-Section. **(g,h)** indicate the width error of 10-Section.

The measurement error of the width of each asparagus stem when equally divided into 4 sections is shown in Figure 20a. For short green asparagus, the error produced by the depth camera sensor when detecting the top and bottom points was relatively small (green area, approximately 6–8%). Therefore, the position error of the left and right key points of each contour section of the asparagus stem was relatively small. When the detection target was taller, the error of the sensor for the top and bottom points of the asparagus stem increased, inevitably causing an increase in the error of the key points of each section. Moreover, due to the smaller number of sections, the mean error and standard deviation also increase relatively (yellow area, 12%). Figure 20b more clearly reflects that the error increases as the asparagus stem grows, and the trend line of the standard deviation of the width of the asparagus stem showed a gentle growth. This deviation could be explained by the hardware issues of the depth camera sensor itself.

The measurement error of the width of each asparagus stem when equally divided into 10 sections is shown in Figure 20g. The green area indicates that the errors are relatively low (approximately 6–8%) on asparagus stalks of different lengths. However, an examination of the standard deviation trend line in Figure 20h revealed no discernible pattern when comparing the section of tall and thick green asparagus with that of shorter specimens, as seen between samples No. 1 and No. 2 versus No. 10 and No. 12. Consequently, this methodology was more advantageous for achieving optimal fitting in tall and thick green asparagus, thereby facilitating the establishment of a more accurate visualization model. Figure 20c–f illustrates the errors associated with segmenting the asparagus stems into 6 and 8 equal sections. These results fall within the range observed for 4 and 10 sections. Given the relatively straight morphology of green asparagus stems and their inherent correlation between length and width, it could be inferred that measurements taken for width were essentially consistent with those taken for length.

3.3.3. Field Test Results

A test was performed to evaluate the visualization of the spatial location information of clustered green asparagus in a laboratory farm environment. Ten sets of green asparagus images (ranging from 40 to 50 green asparagus) were randomly selected from the sunny and cloudy datasets, respectively. And then, the actual length of the green asparagus stems and the depth of the distance from the camera were measured based on the point cloud. The effects of adaptive-section modeling for some sampled asparagus stems (with the bottom occluded, the middle occluded, and the top occluded) are shown in Figure 21.

To evaluate the length error of green asparagus stems (L_{est} , cm), it was necessary to know the coordinates (pixels px) of the top point on the stem (u_{top}, u_{top}) and the bottom point on the ground (v_{bottom}, v_{bottom}), as well as the actual length measured on the point cloud (L_{gt} , cm). After these 20 sets of green asparagus images were modeled by YS3AM, we converted the pixel coordinates of the top and bottom points of the stems in the model to 3D coordinates under the camera coordinate system, which were the top point ($x_{top}, y_{top}, z_{top}$) and the bottom point ($x_{bottom}, y_{bottom}, z_{bottom}$), respectively. Then, based on the research methods in Section 2.6, the model-estimated lengths of green asparagus (L_{est} , the lengths of all detectable green asparagus stems in each image) were compared with the actual lengths measured by the point cloud (L_{gt}), where gt represents the ground truth measurement. Pearson's coefficient, R^2 , and Root Mean Square Error (RMSE) were used to compare the differences between the model-estimated stem lengths and the actual lengths.

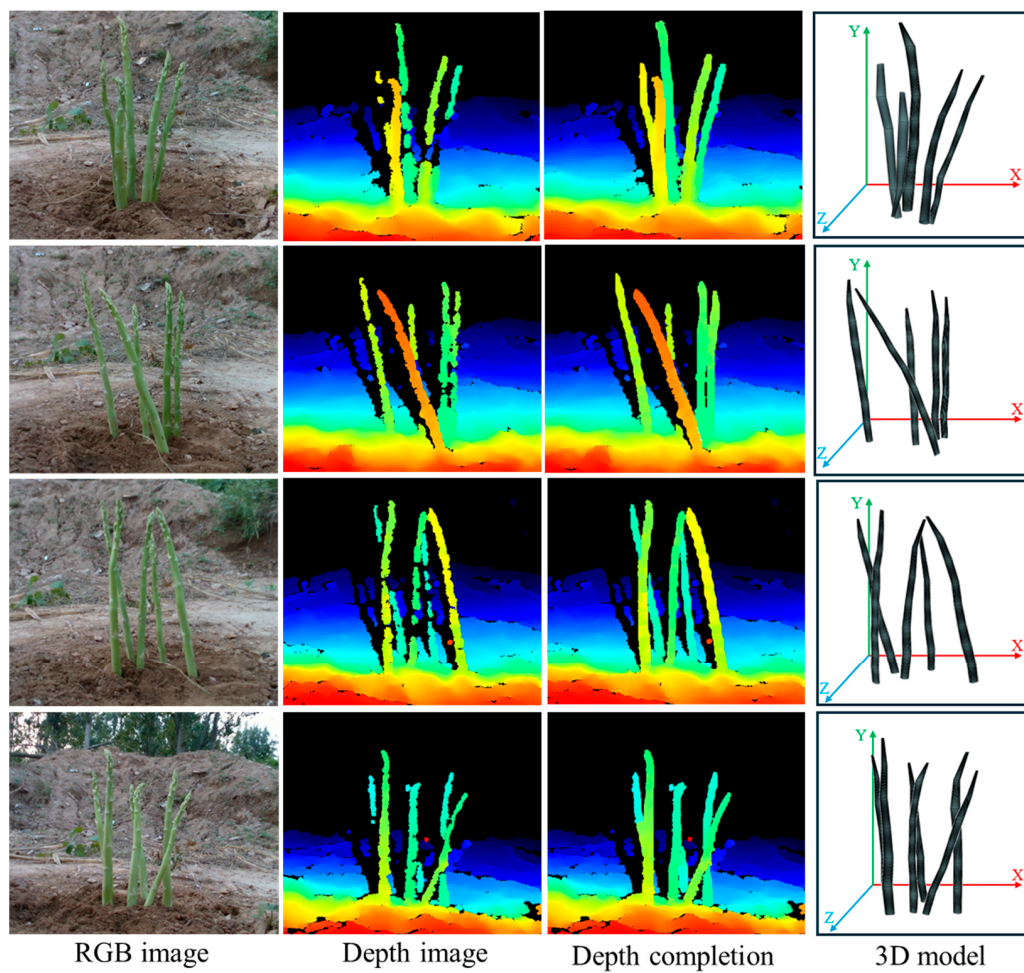


Figure 21. Adaptive-section modeling of green asparagus.

To further determine the accuracy of the spatial information of green asparagus, the lowest ($x_{bottom}, y_{bottom}, z_{bottom}$) and highest ($x_{top}, y_{top}, z_{top}$) points on the ground of each recognized green asparagus stem were taken to test the depth values with the binocular camera in the Z-axis direction, respectively. Subsequently, Pearson's coefficient, R^2 , and RMSE were also used to evaluate the model test results and the actual point cloud measurements.

As can be seen from Table 8, in the Sunny dataset, a total of 54 green asparagus were labeled in 10 groups of data, and 40 were detected, with a detection rate of 74.07%. In the Cloudy dataset, a total of 49 green asparagus were labeled in 10 sets of data tested, and 34 green asparagus were detected, with a detection rate of 67.35%. The true positive detection rate of the Sunny environment is 9.98% higher than that of the Cloudy dataset. The detection effect of the Sunny dataset is better than that of the Cloudy dataset, which was probably due to the image matching error caused by the change in natural light angle and light intensity. By comparing the spatial visualization results of green asparagus identified under two lighting cases, it was not difficult to find that the depth error of the bottom point in the Sunny dataset was much smaller than that in the Cloudy dataset ($0.11 \text{ cm} < 0.26 \text{ cm}$), and the percentage of error was also much smaller than that in the Cloudy dataset ($0.25\% < 0.68\%$). Similarly, the depth error of the top point of the stem in the Sunny dataset was smaller than that in the Cloudy dataset ($0.90 \text{ cm} < 1.87 \text{ cm}$), and the percentage error was also much smaller than that in the Cloudy dataset ($2.62\% < 3.22\%$).

Table 8. Comparison of asparagus detection results with two different datasets.

Imaging Method	Label Asparagus Count	True Positive (Correctly Detected)		Length Error (cm)	Length Error (%)	Bottom Depth Error (cm)	Bottom Depth Error (%)	Top Depth Error (cm)	Top Depth Error (%)
		Asparagus Number	Accuracy (%)						
Sunny	54	40	74.07	0.55	2.07	0.11	0.25	0.90	2.62
Cloudy	49	34	67.35	0.63	2.84	0.26	0.68	1.87	3.22

The length results of asparagus stem estimated by the model in both the Sunny and Cloudy datasets and the actual value measured in the field are shown in Figure 22. In the Sunny dataset, the R^2 , RMSE and Pearson's coefficient of the green asparagus stem length were 0.97, 0.71 and 0.99, respectively (Figure 22a). Following a similar pattern in the Cloudy dataset, the R^2 , RMSE, and Pearson's coefficient were 0.91, 0.77, and 0.91 for green asparagus stem length, respectively (Figure 22b). Overall, both light cases tended to overestimate or underestimate the size of the actual green asparagus, mainly due to light and surrounding background distortion. However, in all cases, the overestimated and underestimated green asparagus lengths compensated for each other, resulting in a slope close to 1:1 between the YS3AM estimated length and the actual measured length (the regression slopes ranging from 0.99 to 1.01).

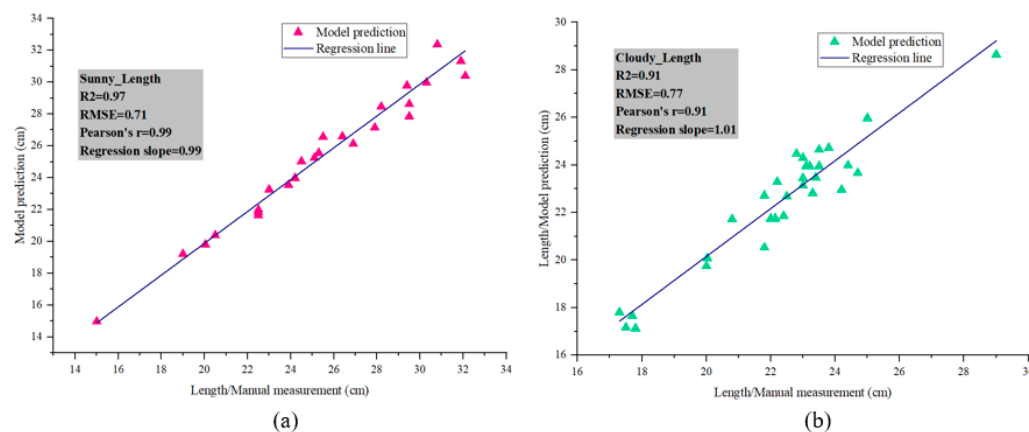


Figure 22. The YS3AM estimation of green asparagus length (L_{est}) using (a) Sunny and (b) Cloudy datasets and comparison to the lengths of green asparagus (L_{gt}) measured manually on the ground. The shaded area indicates the size of the confidence interval for the regression estimates.

The depth comparison results of the bottom points and top points of the asparagus stem estimated by the model in both datasets with the real value measured in the field are shown in Figure 23. In the Sunny dataset, the R^2 , RMSE, and Pearson's coefficient of the bottom depth estimation were 0.96, 0.96, and 0.98, respectively (Figure 23a), while the R^2 , RMSE, and Pearson's coefficient of the top depth estimation were 0.836, 7.44, and 0.915, respectively (Figure 23c). In the Cloudy dataset, the R^2 , RMSE and Pearson's coefficient of the bottom depth were 0.76, 1.25 and 0.87, respectively (Figure 23b); the R^2 , RMSE and Pearson's coefficient of the top depth were 0.784, 4.435 and 0.889, respectively (Figure 23d). The slope between estimated bottom depth distance from the camera and the actual measured distance was slightly different in the two lighting environments, with a slope of 0.91 for the Sunny dataset and 0.62 for the Cloudy dataset. The slopes of the top point in the two light cases were 0.94 and 0.907, respectively. It was clear that the estimated depth values for the green asparagus all deviated from the actual measurements and were more prominent in the Cloudy dataset. This was because in the Cloudy dataset, the light intensity was not large, the color of the end of the stem was dark, and the color was like the

land, and the image distortion was serious. As for the depth test of the highest point, due to the gradual thinning of the stem from bottom to top, the discernible area of the sensor in the stem tip became smaller, the gradient of depth information became steeper, and the data mutation was serious. Affected by the accuracy and error of the sensor, the detection error became larger.

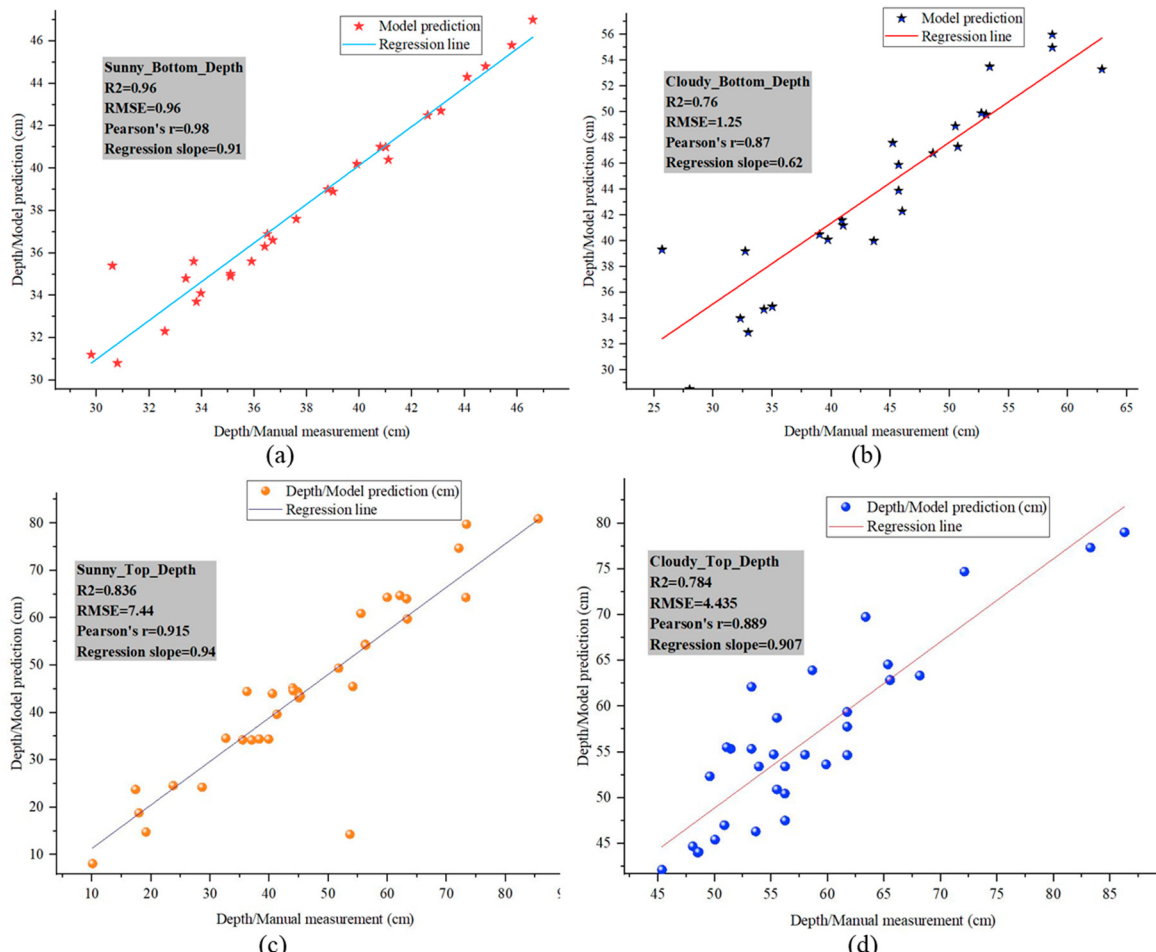


Figure 23. YS3AM estimated the ground lowest points of green asparagus stem in (a) Sunny and (b) Cloudy datasets and compared them with the manual measurements. And it estimated the highest points of the stem in (c) Sunny and (d) Cloudy datasets, comparing these as well with the manual measurements. The shaded area indicates the size of the confidence interval for the regression estimates.

Although the detection of clustered green asparagus in the Sunny dataset might be the best solution for building 3D models, the effects caused by light and the hardware of the sensor cannot be completely ignored, even in manually managed greenhouses. The YS3AM could optimize the detection of clustered green asparagus by obtaining a larger sensing field at different scales and combining the CA-attention mechanism to optimize the detection of outdoor occluded objects. The Cloudy dataset led to a decrease in the resolution of some image regions, and the distortion problem might be the main reason for the decrease in the detection accuracy of deep neural networks. In this paper, the detection of clustered green asparagus in the Sunny dataset was slightly better than in the Cloudy dataset. However, for harvesting under outdoor natural light conditions, the results of both methods were satisfactory.

4. Limitations and Future Work

While YS3AM offers an effective approach for 3D modeling of green asparagus, several improvements are needed to enhance its robustness and generalization across different environments and crop types:

(1) Camera Limitations and Field Deployment

The Intel RealSense D435i RGB-D camera, employed in this study, encounters challenges when dealing with textureless objects like asparagus, which can affect depth accuracy. Additionally, the need for close-range imaging and small variations in camera angle, especially in dynamic field conditions, can impact performance. Future work will focus on enhancing camera calibration, integrating multi-sensor fusion (e.g., LiDAR), and improving system robustness to variations in camera angle and terrain.

(2) Occlusion Handling and Segmentation

While the system performs well in detecting and segmenting individual asparagus stems in less cluttered environments, further refinement is required to improve occlusion handling in densely packed, clustered asparagus. This includes better segmentation accuracy in clustered scenarios and under challenging lighting conditions.

(3) Generalization to Varied Environmental Conditions and Crop Types

The system has been validated in diverse lighting conditions, but its performance under highly dynamic and unpredictable outdoor conditions (e.g., varying light intensity, shadows, and environmental noise) needs further validation. Additionally, while the current work focuses on green asparagus, the model's adaptability to other crop types with different stem shapes or growth patterns should be explored. This may require dataset expansion and algorithm adjustments.

Future research will focus on enhancing the robustness and adaptability of the YS3AM approach, particularly in improving occlusion handling and segmentation accuracy in densely packed environments. Efforts will also be directed toward optimizing system calibration and improving its resilience to variations in camera angle, terrain, and lighting conditions, with validation under diverse outdoor conditions to increase its generalizability. A major direction of future work will be exploring dynamic harvesting in non-stationary environments, examining the impact of camera shake and movement on model accuracy, and optimizing the algorithm for better robustness in dynamic settings. Additionally, we aim to extend the applicability of the YS3AM model to other crop types, especially those with varying geometric shapes and texture characteristics.

5. Conclusions

To accurately obtain spatial positioning for an automatic harvesting robot, this paper develops a novel 3D adaptive-section modeling method, YS3AM, to enhance the precision and efficiency of green asparagus harvesting, filling the gap in previous research. This model achieves precise segmentation of individual asparagus stems in RGB-D images and utilizes a voxel-based modeling approach, combining binary masks and depth maps, to reconstruct 3D models of green asparagus, which offers a viable pathway for real-time 3D modeling in harvesting robots for green asparagus. The conclusions are as follows:

- (1) YS3AM demonstrates stable performance under varying lighting, with improved results on sunny days. Ablation tests show that YS3AM increased precision by 0.81%, recall by 1.73%, mAP by 1.88%, F1 score by 1.27%, and reduced final loss by 0.032 over YOLOv7.

- (2) By segmenting asparagus stems into 4–10 sections based on length, the model meets MAX(RMSE_i) requirements, significantly reducing discrepancies between point cloud measurements and model predictions.
- (3) Field tests show that adaptive section based on asparagus length provided a strong fit, with average RMSE in length (0.74) and bottom depth (1.105) under varied lighting.
- (4) YS3AM achieves near-real-time detection with an average image processing time of 22 ms, making it suitable for deployment in the Robot Operating System (ROS).

In conclusion, the YS3AM method significantly advances the field of 3D modeling for green asparagus harvesting, providing a robust solution for real-time, precise spatial positioning. This work not only enhances the segmentation accuracy of individual asparagus stems under varying environmental conditions but also integrates advanced voxel-based modeling techniques to generate accurate 3D reconstructions. While further improvements are needed to handle dynamic harvesting scenarios and improve robustness to field conditions, the results of this study highlight the potential of YS3AM for deployment in autonomous harvesting robots. Future work will focus on addressing these challenges, broadening the model’s adaptability to other crop types, and optimizing the system for real-time dynamic environments, paving the way for more efficient and reliable agricultural robotics.

Author Contributions: S.M.: Writing—original draft, Methodology, Data curation, Validation, Software. J.L.: Methodology, Investigation, Data curation, Validation. P.Z.: Methodology, Investigation, Validation. J.Y.: Writing—Review and Editing, Conceptualization, Funding acquisition, Supervision. X.L.: Methodology, Investigation, Resources, Project administration. All authors have read and agreed to the published version of the manuscript.

Funding: This work was supported by National Natural Science Foundation of China (52275262) and Cotton Industry Technology System and Industrial Innovation Team Projects in Shandong Province (SDAIT-03-09).

Data Availability Statement: The data presented in this study are available on request from the corresponding author. The data are not publicly available due to the nature of our data, which involve proprietary information, and potential intellectual property implications.

Conflicts of Interest: The authors declare no conflicts of interest.

References

1. Clary, C.D.; Ball, T.; Ward, E.; Fuchs, S.; Durfey, J.E.; Cavalieri, R.P.; Folwell, R.J. Performance and Economic Analysis of a Selective Asparagus Harvester. *Appl. Eng. Agric.* **2007**, *23*, 571–577. [[CrossRef](#)]
2. Chen, M.; Tang, Y.; Zou, X.; Huang, Z.; Zhou, H.; Chen, S. 3D global mapping of large-scale unstructured orchard integrating eye-in-hand stereo vision and SLAM. *Comput. Electron. Agric.* **2021**, *187*, 106237. [[CrossRef](#)]
3. Liu, M.; Jia, W.; Wang, Z.; Niu, Y.; Yang, X.; Ruan, C. An accurate detection and segmentation model of obscured green fruits. *Comput. Electron. Agric.* **2022**, *197*, 106984. [[CrossRef](#)]
4. Bac, C.W.; Henken, E.J.V.; Hemming, J.; Edan, Y. Harvesting Robots for High-value Crops: State-of-the-art Review and Challenges Ahead. *J. Field Robot.* **2014**, *31*, 888–911. [[CrossRef](#)]
5. Bargoti, S.; Underwood, J. Deep Fruit Detection in Orchards. *arXiv* **2016**, arXiv:1610.03677.
6. Dorj, U.-O.; Lee, M.; Yun, S.-S. An yield estimation in citrus orchards via fruit detection and counting using image processing. *Comput. Electron. Agric.* **2017**, *140*, 103–112. [[CrossRef](#)]
7. Kondo, N.; Ting, K.C. Robotics for Plant Production. *Artif. Intell. Rev.* **1998**, *12*, 227–243. [[CrossRef](#)]
8. Irie, N.; Taguchi, N.; Horie, T.; Ishimatsu, T. Asparagus harvesting robot coordinated with 3-D vision sensor. In Proceedings of the IEEE International Conference on Industrial Technology, Churchill, VIC, Australia, 10–13 February 2009.
9. Sakai, H.; Shiigi, T.; Kondo, N.; Ogawa, Y.; Taguchi, N. Accurate Position Detecting during Asparagus Spear Harvesting using a Laser Sensor. *Eng. Agric. Environ. Food* **2013**, *6*, 105–110. [[CrossRef](#)]
10. Zheng, Y.Y.; Kong, J.L.; Jin, X.B.; Wang, X.Y.; Zuo, M. CropDeep: The Crop Vision Dataset for Deep-Learning-Based Classification and Detection in Precision Agriculture. *Sensors* **2019**, *19*, 1058. [[CrossRef](#)]

11. Peebles, M.; Lim, S.H.; Duke, M.; McGuinness, B. Investigation of Optimal Network Architecture for Asparagus Spear Detection in Robotic Harvesting. *IFAC-Pap.* **2019**, *52*, 283–287. [[CrossRef](#)]
12. Ren, S.; He, K.; Girshick, R.; Sun, J. Faster R-CNN: Towards Real-Time Object Detection with Region Proposal Networks. *IEEE Trans. Pattern Anal. Mach. Intell.* **2017**, *39*, 1137–1149. [[CrossRef](#)] [[PubMed](#)]
13. Li, P.; Liu, X.; Li, Y.; Liu, C. Visual Recognition of Green Asparagus in the Field Based on Dual-Channel Threshold Segmentation and CNN. *J. Agric. Mech. Res.* **2021**, *43*, 19–25.
14. Lecun, Y.; Bottou, L.; Bengio, Y.; Haffner, P. Gradient-based learning applied to document recognition. *Proc. IEEE* **1998**, *86*, 2278–2324. [[CrossRef](#)]
15. Hong, W.; Ma, Z.; Ye, B.; Yu, G.; Tang, T.; Zheng, M. Detection of Green Asparagus in Complex Environments Based on the Improved YOLOv5 Algorithm. *Sensors* **2023**, *23*, 1562. [[CrossRef](#)]
16. Wang, X.; Li, W.; Wang, L.; Shi, Y.; Wu, Y.; Wang, D. Method of Detection-Discrimination-Localization for Mature Asparagus Based on Improved YOLACT++ %J Transactions of the Chinese Society for Agricultural Machinery. *Trans. Chin. Soc. Agric. Mach.* **2023**, *54*, 259–271.
17. Li, S.; Zhang, S.; Xue, J.; Sun, H. Lightweight target detection for the field flat jujube based on improved YOLOv5. *Comput. Electron. Agric.* **2022**, *202*, 107391. [[CrossRef](#)]
18. Xiang, R.; Ying, Y.; Jiang, H. Development of Real-time Recognition and Localization Methods for Fruits and Vegetables in Field. *Trans. Chin. Soc. Agric. Mach.* **2013**, *44*, 208–223.
19. Leu, A.; Razavi, M.; Langstädter, L.; Ristic-Durrant, D.; Raffel, H.; Schenck, C.; Graser, A.; Kuhfuss, B. Robotic green asparagus selective harvesting. *IEEE/ASME Trans. Mechatron.* **2017**, *22*, 2401–2410. [[CrossRef](#)]
20. Kennedy, G.; Ila, V.; Mahony, R. A Perception Pipeline for Robotic Harvesting of Green Asparagus. *IFAC-Pap.* **2019**, *52*, 288–293. [[CrossRef](#)]
21. Mu, S.; Dai, N.; Yuan, J.; Liu, X.; Xin, Z.; Meng, X. S2CPL: A novel method of the harvest evaluation and subsoil 3D cutting-Point location for selective harvesting of green asparagus. *Comput. Electron. Agric.* **2024**, *225*, 109316. [[CrossRef](#)]
22. Hu, K.; Chen, Z.; Kang, H.; Tang, Y. 3D vision technologies for a self-developed structural external crack damage recognition robot. *Autom. Constr.* **2024**, *159*, 105262. [[CrossRef](#)]
23. Yoshida, T.; Kawahara, T.; Fukao, T. Fruit recognition method for a harvesting robot with RGB-D cameras. *ROBOMECH J.* **2022**, *9*, 15. [[CrossRef](#)]
24. Ma, Z.; Wan, H.; Gan, X. Research on Crop 3D Model Reconstruction Based on RGB-D Binocular Vision. *Sci. Program.* **2023**, *2023*, 5974981. [[CrossRef](#)]
25. Magistri, F.; Marks, E.; Nagulavancha, S.; Vizzo, I.; Läbe, T.; Behley, J.; Halstead, M.; McCool, C.; Stachniss, C. Contrastive 3D Shape Completion and Reconstruction for Agricultural Robots Using RGB-D Frames. *IEEE Robot. Autom. Lett.* **2022**, *7*, 10120–10127. [[CrossRef](#)]
26. Omasa, K.; Qiu, G.Y.; Watanuki, K.; Yoshimi, K.; Akiyama, Y.J.E.S. Accurate estimation of forest carbon stocks by 3-D remote sensing of individual trees. *Environ. Sci. Technol.* **2003**, *37*, 1198–1201. [[CrossRef](#)]
27. Herrero-Huerta, M.; Lindenbergh, R.; Gard, W. Leaf movements of indoor plants monitored by terrestrial LiDAR. *Front. Plant Sci.* **2018**, *9*, 189. [[CrossRef](#)] [[PubMed](#)]
28. Bloice, M.D.; Stocker, C.; Holzinger, A. Augmentor: An Image Augmentation Library for Machine Learning. *arXiv* **2017**, arXiv:1708.04680. [[CrossRef](#)]
29. Wang, C.-Y.; Bochkovskiy, A.; Liao, H.-Y.M. YOLOv7: Trainable bag-of-freebies sets new state-of-the-art for real-time object detectors. *arXiv* **2022**, arXiv:2207.02696.
30. Anasosalu Vasu, P.K.; Gabriel, J.; Zhu, J.; Tuzel, O.; Ranjan, A. MobileOne: An Improved One Millisecond Mobile Backbone. *arXiv* **2022**, arXiv:2206.04040.
31. Hou, Q.; Zhou, D.; Feng, J. Coordinate Attention for Efficient Mobile Network Design. *arXiv* **2021**, arXiv:2103.02907.
32. Dosovitskiy, A.; Beyer, L.; Kolesnikov, A.; Weissenborn, D.; Zhai, X.; Unterthiner, T.; Dehghani, M.; Minderer, M.; Heigold, G.; Gelly, S.; et al. An Image is Worth 16x16 Words: Transformers for Image Recognition at Scale. *arXiv* **2020**, arXiv:2010.11929.
33. Kirillov, A.; Mintun, E.; Ravi, N.; Mao, H.; Rolland, C.; Gustafson, L.; Xiao, T.; Whitehead, S.; Berg, A.C.; Lo, W.-Y.; et al. Segment Anything. *arXiv* **2023**, arXiv:2304.02643.
34. He, K.; Chen, X.; Xie, S.; Li, Y.; Dollár, P.; Girshick, R. Masked Autoencoders Are Scalable Vision Learners. *arXiv* **2021**, arXiv:2111.06377.
35. Ku, J.; Harakeh, A.; Waslander, S.L. In Defense of Classical Image Processing: Fast Depth Completion on the CPU. *arXiv* **2018**, arXiv:1802.00036.

Disclaimer/Publisher’s Note: The statements, opinions and data contained in all publications are solely those of the individual author(s) and contributor(s) and not of MDPI and/or the editor(s). MDPI and/or the editor(s) disclaim responsibility for any injury to people or property resulting from any ideas, methods, instructions or products referred to in the content.